



**DEVELOPMENT OF IN-PLANE SURFACE DEFORMATION SENSING FOR THIN
FILM PVDF ACTUATED MEMBRANE MIRRORS**

THESIS

John J. Cornelius, Captain, USAF

AFIT/GA/ENY/06-M01

**DEPARTMENT OF THE AIR FORCE
AIR UNIVERSITY**

AIR FORCE INSTITUTE OF TECHNOLOGY

Wright-Patterson Air Force Base, Ohio

APPROVED FOR PUBLIC RELEASE; DISTRIBUTION UNLIMITED

The views expressed in this thesis are those of the author and do not necessarily reflect the official policy or position of the United States Air Force, Department of Defense or United States Government.

AFIT/GA/ENY/06-M01

Development of In-Plane Surface Deformation Sensing for Thin Film PVDF Actuated
Membrane Mirrors

THESIS

Presented to the Faculty

Department of Aeronautical and Astronautical Engineering

Graduate School of Engineering and Management

Air Force Institute of Technology

Air University

Air Education and Training Command

In Partial Fulfillment of the Requirements for the
Degree of Master of Science in Astronautical Engineering

John J Cornelius, B.S.E.

Captain, USAF

March 2005

APPROVED FOR PUBLIC RELEASE; DISTRIBUTION UNLIMITED

AFIT/GA/ENY/06-M01

Development of In-Plane Surface Deformation Sensing for Thin Film PVDF Actuated
Membrane Mirrors

John J. Cornelius, B.S.E

Captain, USAF

Approved:

Dr. Richard G. Cobb
Chairman

date

Dr. Anthony N. Palazotto
Member

date

Lt Col Matthew Goda
Member

date

Abstract

This study investigated the feasibility of surface deformation sensing of a membrane mirror using only embedded PVDF sensors. Results were compared to measured deformations using a scanning laser vibrometer. The frequency response function (FRF) was measured based on recorded voltages of a single-layer 7-sensor mirror actuated externally from the embedded PVDF actuators. Additionally, a two-layer, 7-sensor, 7-actuator membrane mirror was constructed for use, with one layer acting as the sensing layer and the other acting as the actuation layer. The measured FRF for this mirror was compared to previous results. Finally a single-layer 61-sensor PVDF mirror was constructed to experimentally investigate the practicality of denser sensor/actuators patterns. Experimental results for all configurations are presented.

Acknowledgements

First and foremost, I would like to thank my wife. Without her continued support and dedication I would not have achieved what I have in life. Thank you for supporting me through everything. Secondly, I would like to acknowledge my two boys. They have done their best to keep my focus balanced while I have put in the long hours required of this research.

Special thanks go to Dr. Richard Cobb (AFIT/ENY) for his guidance and motivation throughout the course of this project. I would also like to thank Maj Michael Shepherd (AFIT/ENY), Maj Laverne Starman (AFIT/ENG), Bill Trop (AFIT/ENG), Dr. Anthony Palazotto (AFIT/ENY), and Lt Col Matthew Goda (AFIT/ENG) for their support of this effort. One last person I would like to thank is Capt Gina Peterson. We spent many long hours in the lab together trying to make things work, and I appreciate her tireless dedication to this project.

Finally, for the continued financial support from which this project benefits, I would like to thank Lt. Col. Sharon Heise at the Air Force Office of Scientific Research.

Capt John J. Cornelius

Table of Contents

<i>Abstract</i>	iv
<i>Acknowledgements</i>	v
<i>Table of Contents</i>	vi
<i>List of Figures</i>	ix
<i>List of Tables</i>	xii
<i>List of Tables</i>	xii
I. Introduction.....	1
1.1 Overview.....	1
1.2 Scope.....	2
1.3 Problem.....	3
1.4 Summary of Thesis.....	4
II. Review of Relevant Literature.....	5
2.1 Overview.....	5
2.2 Deformable membrane-like structures.....	6
2.2.1 Sensing Schemes.....	6
2.2.2 Actuation Schemes.....	10
III. Development of Sensing Method.....	14
3.1 Overview.....	14
3.2 Theoretical Development.....	15
3.2.1 FRF Development.....	16
3.2.2 State Space Realization.....	18
3.2.3 Determining Zernike Shapes from Output Voltage.....	20

3.3 Fabrication	29
3.4 Testing.....	32
3.4.1 Test Overview.....	32
3.4.2 Laser Vibrometer test.....	32
3.4.3 Patch Output	33
3.5 Results.....	35
3.5.1 Results Overview.....	35
3.5.2 Discussion of Results	35
IV. Development of 61-Patch Mirror.....	46
4.1 Overview.....	46
4.2 Control Pattern Design.....	47
4.3 Fabrication Process	49
4.4 Tensioning and Mounting.....	52
V. Testing of 61-Patch Mirror	55
5.1 Overview.....	55
5.2 Patch Measurement Test.....	55
5.3 Laser Vibrometer Test	62
VI. Conclusion and Recommendations.....	65
6.1 Overview of Experiment.....	65
6.1.1 Sensing Method.....	65
6.1.2 Development of 61-Patch Mirror.....	65
6.1.3 Testing of 61-Patch Mirror.....	66
6.2 Conclusions Drawn.....	66

6.2.1 Sensing Method.....	66
6.2.2 Development of 61-Patch Mirror.....	66
6.2.3 Testing of 61-Patch Mirror.....	67
6.3 Areas for Further Development.....	67
6.3.1 Sensing Method.....	68
6.3.2 61-Patch Mirror.....	68
6.4 Summary.....	69
Appendix A: Matlab Code for Generating Mode Shapes.....	70
A.1 Plate Equation Mode Shapes.....	70
A.2 Membrane Equation Mode Shapes.....	71
Appendix B: Additional Plots.....	72
<i>Bibliography</i>	74
<i>Vita</i>	76

List of Figures

Figure 1: Comparison of Hubble Images Before (left) and After (right) COSTAR (7)..... 5

Figure 2: Layout of Wave-front Sensing Setup at AFIT 7

Figure 3: Layout of Wave-front Sensing Setup used at Universite Denis-Dederot (4)..... 8

Figure 4: Setup of Wave-front Generator Method (1)..... 9

Figure 5: Setup of the Interferometer Method (1) 10

Figure 6: Design of a Unimorph System (21)..... 12

Figure 7: Possible Control System for Deformable Mirror 14

Figure 8: Flowchart Depicting Theoretical Development 15

Figure 9: Mode Shapes from Plate Equation ($m=0$)..... 25

Figure 10: Mode Shapes from Plate Equation ($m=1$)..... 25

Figure 11: Mode Shapes from Plate Equation ($m=2$)..... 26

Figure 12: Mode Shapes from Plate Equation ($m=3$)..... 26

Figure 13: Mode Shapes from Membrane Equation ($m=0$)..... 27

Figure 14: Mode Shapes from Membrane Equation ($m=1$)..... 28

Figure 15: Mode Shapes from Membrane Equation ($m=2$)..... 28

Figure 16: Mode Shapes from Membrane Equation ($m=3$)..... 29

Figure 17: Test Setup for Laser Vibrometer Test..... 33

Figure 18: Layout of 7-Patch Mirror Showing Location of Each Patch..... 34

Figure 19: FRF, Patch 6 input, Patch 6 output..... 36

Figure 20: Difference Between Predicted Shape and Experimental Shape (plate equation, $m=0$,
 $n=1$)..... 37

Figure 21: Difference Between Predicted Shape and Experimental Shape (membrane equation, $m=0, n=1$).....	38
Figure 22: Difference Between Predicted Shape and Experimental Shape (plate equation, $m=2, n=1$).....	39
Figure 23: Difference Between Predicted Shape and Experimental Shape (membrane equation, $m=2, n=1$).....	40
Figure 24: FRF Result From Patch Output Test.....	41
Figure 25: Time Response Showing Output to Five Hertz Sine Wave Input.....	42
Figure 26: Time Response to Five Hertz Sine Wave (zoom view).....	42
Figure 27: Time Response to 10 Hz Sine Wave.....	43
Figure 28: Time Response to 10 Hz Sine Wave (zoom view).....	43
Figure 29: Time Response to a 200-Hz Sine Wave.....	44
Figure 30: Time Response to 200-Hz Sine Wave (zoom view).....	45
Figure 31: 61-Patch Mirror Design.....	47
Figure 32: Mask Used For Transferring Pattern to PVDF.....	49
Figure 33: Wafer Mask Aligner.....	51
Figure 34: Aluminum Ring Design for 3-in. Mirror.....	53
Figure 35: 61-Patch Mirror Without Silicon Coating.....	54
Figure 36: Patches Measured During Test.....	57
Figure 37: Comparison of One-Direction with Another Direction - First Ring.....	58
Figure 38: Comparison of One-Direction with Another Direction - Second Circle.....	58
Figure 39: Comparison of One-Direction with Another Direction - Third Circle.....	59
Figure 40: Comparison of One-Direction with Another Direction - Fourth Circle.....	59

Figure 41: FRF's for Patches 2, 8, 20, and 38	60
Figure 42: FRF's for Patches 5, 14, 29, and 50	61
Figure 43: FRF's for Patches 3, 10, 23, and 42	61
Figure 44: Laser Vibrometer Test Setup.....	62
Figure 45: Close-Up of Mirror in Laser Vibrometer Test Setup	63
Figure 46: Comparison of FRF's From Two Tests	64
Figure 47: FRF's for Patches 4, 12, 26, and 46	72
Figure 48: FRF's for Patches 6, 16, 32, and 54	72
Figure 49: FRF's for Patches 7, 18, 35, and 58	73

List of Tables

Table 1: Physical Properties of Material (10).....	21
Table 2: Numerical Values of Beta.....	23
Table 3: Predicted Natural Frequencies from Plate Equation (Hz)	24
Table 4: Predicted Natural Frequencies from Membrane Equation	27
Table 5: Measured Natural Frequencies (Hz).....	36
Table 6: Percent Difference Between Measured and Predicted Frequencies (plate equation).....	36
Table 7: Percent Difference Between Measured and Predicted Frequencies (membrane equation)	36
Table 8: Pictorial Representation of Zernike Polynomials (13)	46
Table 9: Operational Parameters for Acoustic Source (16).....	56

I. Introduction

1.1 Overview

Imaging from space has recently become a vital element of the United States' war fighting plan. Our military relies on satellite imagery now more than at any other time in our history. It is because of this that it is vital to maintain a premier satellite imaging architecture. One way to assure this is through the development of large aperture space telescopes. The resolution of a satellite imaging system is directly proportional to the diameter of the aperture that collects the light for the telescope. The aperture for most space telescopes consists of a large primary mirror. This mirror is traditionally constructed from polished glass. This has led to the belief that any increase in resolution will carry with it a significant increase in weight.

Recent research has been conducted into making these large mirrors lighter weight. The methods involved include changing the material that is used to construct large mirrors or manufacturing a deployable mirror using a thin-film membrane-like material. One problem associated with the thin-film membrane mirror is the difficulty in controlling it to a certain shape once it is deployed. Mirrors used for optical imaging must have surface aberrations less than a fraction of the wavelength of the light that is being used for imaging. Visible light has a wavelength between 400-700 nm. This means that the mirrors surface must be controlled to the tenth of a micron level. To do this, two things are needed. First, a method of sensing the surface deflections is required. Second, a method of actuating the surface needs to be developed. There are a number of promising materials with which both of these can be accomplished.

Piezoelectric materials exhibit a property whereby they expand when a voltage is applied and also produce a voltage when they are stretched. This property is very useful in developing control systems for membrane mirrors. A mirror that can be manufactured from a piezoelectric

material will be able to sense movement (strain) of its surface. Also, control can be achieved by applying a voltage to actuators built into the mirror. The development of large aperture mirrors for space telescopes requires more advanced research into the use of these piezoelectric membrane materials. With advancements in the fields of manufacturing, control methodology, and optical design, large aperture membrane mirrors will one day be possible.

1.2 Scope

Previous research efforts at the Air Force Institute of Technology have been successful in proving the validity of using piezoelectric materials for the construction of thin-film membrane mirrors (14, 17). The specific material used was Polyvinyl Difluoride (PVDF). This research involved etching control patterns of 7 patches into the PVDF and applying a voltage to individual patches to show a static displacement. Additional research developed a data acquisition system to measure the surface of the mirror in real-time in order to characterize the dynamic actuation of the mirror (17). These efforts all utilized a Shack-Hartmann wave-front sensor in order to measure the deflection of the mirror. This present research endeavors to measure the surface deformation using only the PVDF material without the aid of the wave-front sensor.

A two-layer mirror was constructed so that one layer could be used for sensing and the second could be used for actuation. This enables the eventual control system to be self-contained which would be preferred in a space application. It would be impractical to launch a wave-front sensor with a satellite, to be used in the control system. This research attempts to demonstrate the viability of the PVDF as a sensing device. A modal analysis of the mirror using the patches as sensors was done and compared to modal analyses done with other sensing methods.

The scope of this research is also expanded to involve new manufacturing methods of developing mirrors with a large number of actuators. If the PVDF will be used for sensing the surface as well as actuating, a larger number of patches need to be etched on the surface so that the number of sensors used per surface area will be greater than what has previously been used in research at AFIT. The previous research efforts used a method of hand drawing control patches onto the PVDF and were only able to etch 7 patches. This research demonstrates a method of achieving a 61-patch mirror, which can be used for both sensing and actuation.

1.3 Problem

One concern with previous research efforts was its applicability to space systems. As mentioned previously it would be impractical to take a wave-front sensor into orbit to be used in the control system. Therefore the primary focus of this research is to develop a method of sensing the surface deflection that would be more applicable to spacecraft on orbit. One way to do this would be with sensors embedded within the structure of the mirror itself. This is possible using the piezoelectric characteristics of the PVDF.

A secondary concern, which was brought up as a result of the development of the embedded sensing method, is the need for more than 7 actuators/sensors. Previously these patches had been etched onto the PVDF by hand making it very unrepeatable as well as limiting the amount of patches that could be used. It is very difficult to get precise control of a surface with only 7 patches over a 6-in diameter circle. Therefore a secondary focus of this research involves developing a method of etching a control pattern that contains a significant number of patches. The number of patches chosen for this research was 61 over a 2-in diameter circle in order to enable comparison with a commercially available deformable mirror.

These newly developed methods, if successful, will allow for a more controllable surface without the need for additional equipment. These methods are more applicable to space systems and will be useful to future research efforts that will take place.

1.4 Summary of Thesis

The first chapter provides a brief overview of the subject of this research effort. The scope of the research is provided as well as a formulation of the problem that is being investigated.

The second chapter provides a review of some of the relevant research that has been accomplished in this field of study. This is intended to give the reader a better background to the issues being discussed and in no way constitutes an exhaustive list of all research being conducted.

The third chapter discusses the new sensing method that was developed. This includes a description of how the test subject was manufactured as well as describing the testing that was done and the results achieved. Finally, the modal analysis is discussed and conclusions are drawn.

The fourth chapter provides an extensive description of development of the 61-patch mirror. It describes the design of the control pattern and the process used to etch the surface. Finally, information of tensioning and mounting the mirror is given.

The fifth chapter describes the testing method that was used on the 61-patch mirror. The test setup is given and the results are discussed. The final chapter gives the conclusions of all the tests conducted. It also outlines areas in which future study would be beneficial.

II. Review of Relevant Literature

2.1 Overview

There is a significant amount of research being conducted in the area of deformable mirror technology. Much of this research is focusing on decreasing the areal density of the mirror itself. Areal density is a measurement of mass per surface area and is a good indicator of how large of a mirror can be put into orbit. Mirrors with low areal density have a very low mass, a very large surface area, or some combination of both of these factors. In order to achieve this, researchers are focusing on using materials that can be folded or rolled and then deployed once the system is on orbit.

Folding or rolling materials that will eventually be used as a mirror introduces a number of potential errors in the resulting image. A small deviation from the ideal surface can create aberrations that will drastically decrease the utility of the image. This is evident from the images taken by the Hubble Space telescope before and after the COSTAR package was installed (7). Figure 1 shows a comparison between an image taken before the correction was installed to an image taken after the correction was installed.



Figure 1: Comparison of Hubble Images Before (left) and After (right) COSTAR (7)

Abberations such as this can be introduced into a system upon deployment and during normal operations. It is because of this that active control is needed to maintain the surface shape of the mirror.

Research of control systems has focused on two different aspects. These two aspects are both essential to the final control solution. The first of these aspects is a method of sensing the deformation of the mirror surface. This must be a method that can be conducted on orbit so that displacement information can be fed back to the controller. The second aspect is a method of actuating the surface in order to achieve the desired shape.

2.2 Deformable membrane-like structures

2.2.1 Sensing Schemes

A number of different methods of sensing the mirror surface have been tried. Research at AFIT has made use of a Shack-Hartmann wave-front sensor in order to detect movement of the mirror surface. This sensor divides the entire mirror surface into sub-apertures. It then uses a laser to focus a light on each of these sub-apertures. As the surface deforms this focus point moves from its original location. The sensor then measures the new locations of each of these focus points and then calculates a gradient for each of the sub-apertures. Computer algorithms can then be used to compute surface deformations, optical path difference, Zernike polynomials, or a number of other methods for describing the surface.

Researchers at the Universite Denis-Diderot in Paris are also using a Shack-Hartmann wave-front sensor with a deformable mirror in order to image the human eye (4). Shack-Hartmann sensing will give a very accurate portrayal of the surface but is unrealistic when

considered for use in space. The primary reason for this is the extent of the setup required for the equipment to work properly. As can be seen from Figure 2 and Figure 3 there is a significant amount of equipment needed which would be unfeasible to put on a spacecraft in orbit.

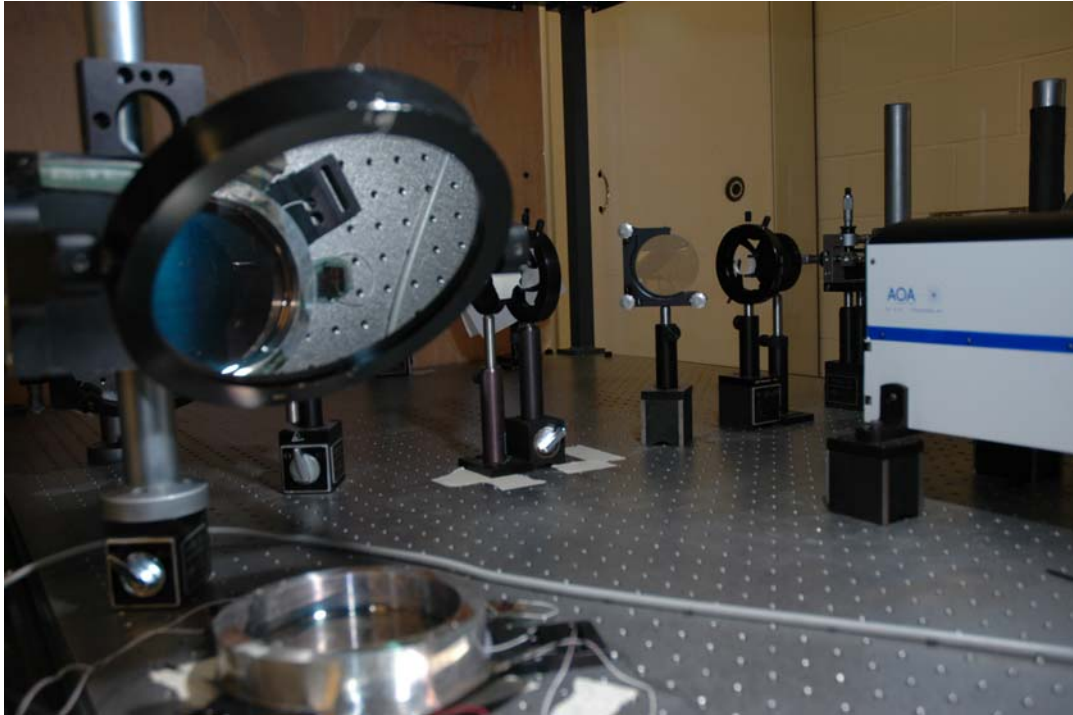


Figure 2: Layout of Wave-front Sensing Setup at AFIT

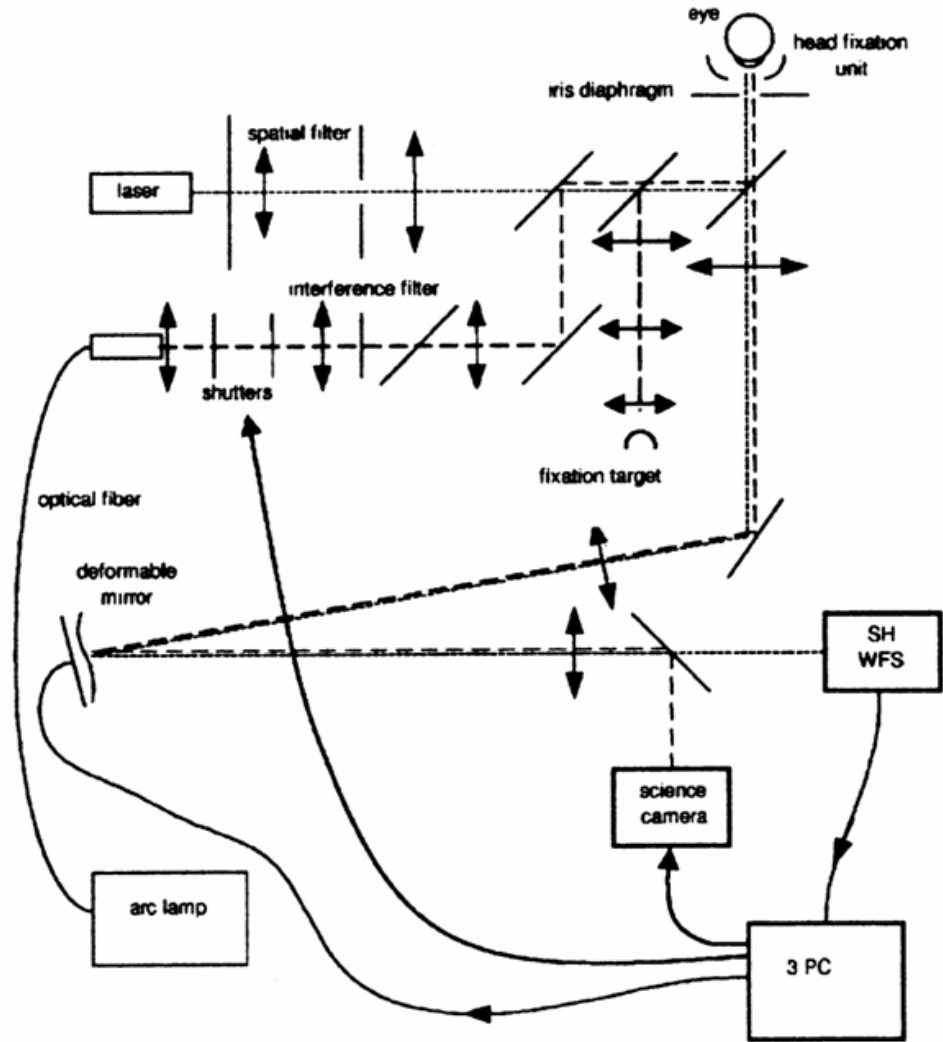


Figure 3: Layout of Wave-front Sensing Setup used at Universite Denis-Dederot (4)

Researchers in an article published in *Applied Optics* (1), demonstrated two different methods of characterizing the surface of a deformable mirror without the use of a wave-front sensor. The first of these methods involves the use of a wave-front generator and a single photo detector. An iterative approach is used to train the mirror to adapt to variations in the wave-front. Figure 4 shows the setup of this method.

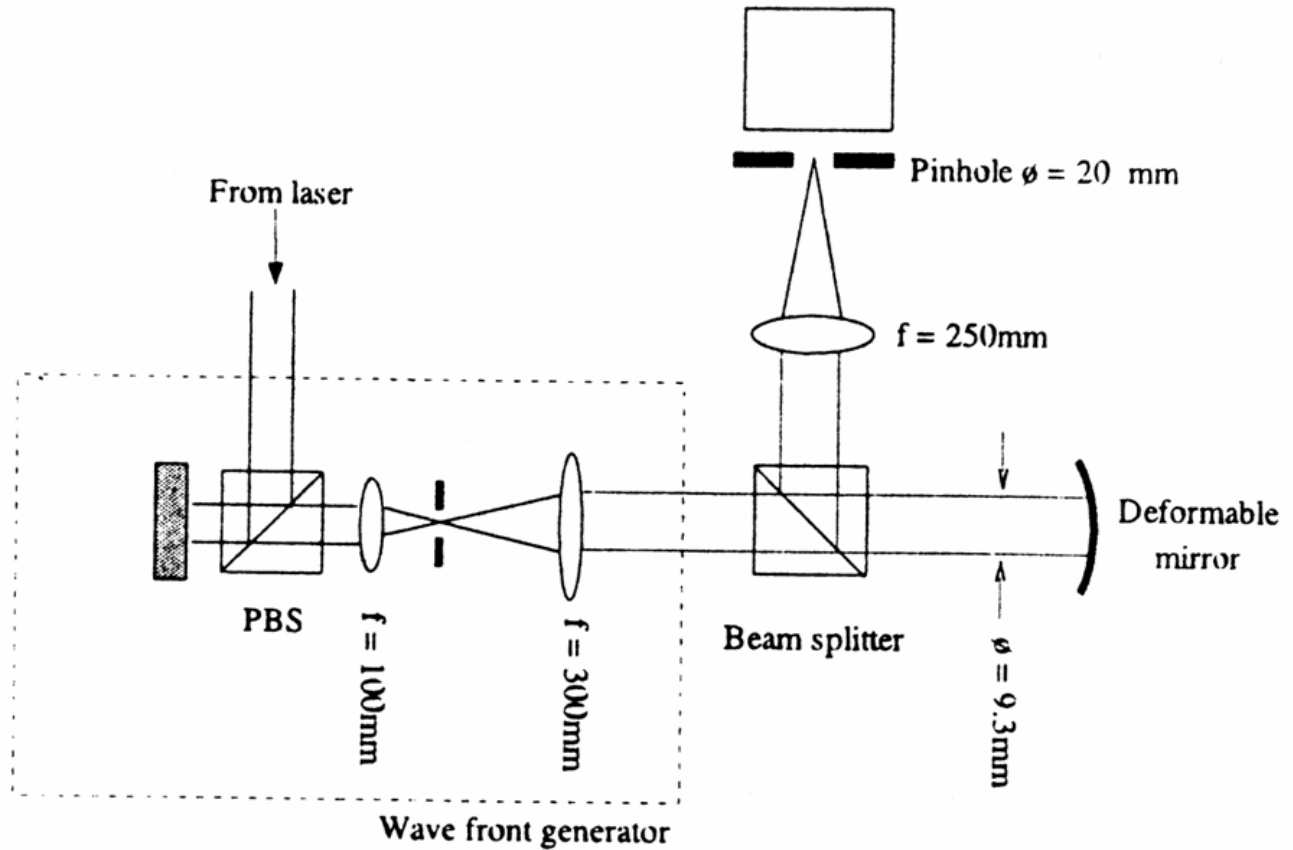


Figure 4: Setup of Wave-front Generator Method (1)

This method computes a matrix relating the control signals required to a modal basis, usually Zernike polynomials. The signal going in to the photo detector (APD) is measured and an iterative process is used to calculate the required control signal to maximize this signal. The result is a matrix that relates the control signal to the Zernike polynomials that describe the wave-front (1). This method would likely not hold up in a space application either because of the data required as well as the time required to do the iterations. This method has no apparent advantages over Shack-Hartmann sensing.

The second method proposed by these researchers is one that utilizes an interferometer and fringe pattern analysis. Figure 5 shows the setup of the optical train of this method.

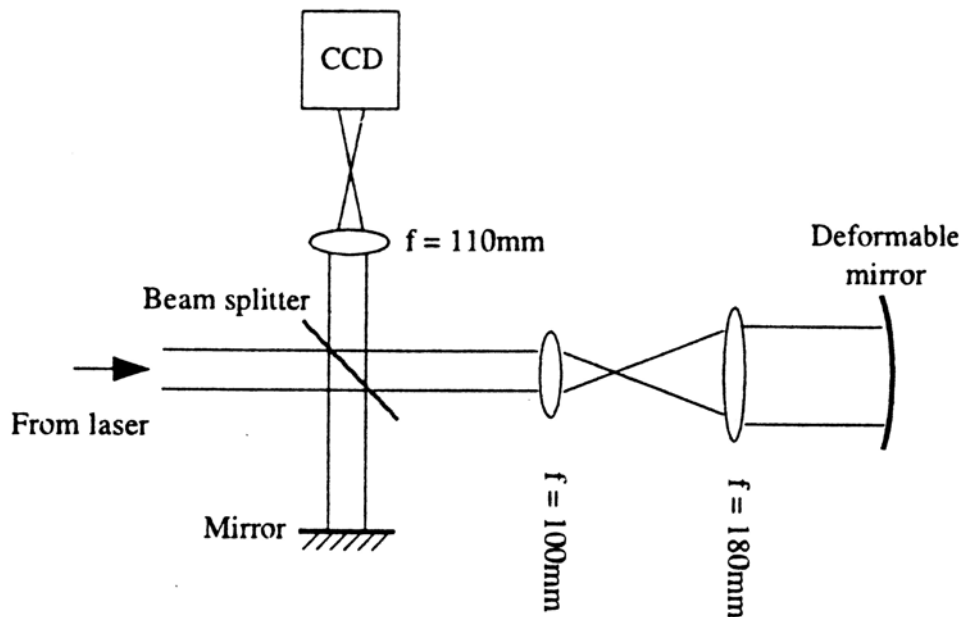


Figure 5: Setup of the Interferometer Method (1)

This method places the deformable mirror in one arm of a Twyman-Green interferometer. The data from the interferometer is then analyzed using fringe pattern analysis and phase unwrapping. The phase introduced by the deformable mirror is contained entirely within the fringe pattern measured by the interferometer. Once this phase is determined a control scheme is fairly straight forward and can be calculated using a number of different basis sets (1). This method shows much promise for space applications. The optical path is relatively simple and interferometers are used already in some space applications. This also does not require a reference light source such as the wave-front sensor and the wave-front generator methods do. Further research on this method is required to demonstrate its applicability to space systems.

2.2.2 Actuation Schemes

There have been many significant contributions by researchers to the area of actuating deformable mirrors. Vdovin, Loktev, and Simonov, from OKO technologies in the Netherlands,

have summarized these various actuation schemes. The first of the actuation schemes mentioned by these authors is a deformable substrate. This design consists of a base substrate with discrete axial actuators attached to it. Attached to the actuators is a deformable substrate. Each of the actuators is able to act independently and push or pull the deformable substrate in order to achieve out of plane motion (18).

The second method of actuation is the bimorph design. This design consists of two sheets of piezoelectric material, bonded together and bonded to a membrane-like structure that will act as the mirror. The sheets are aligned such that when a voltage is applied to the piezoelectric material one of the sheets stretches and the other contracts thus creating a bending motion. This bending motion then results in an out-of-plane displacement for the mirror surface (18). A variation on this design is the unimorph mirror, which has been the subject of research at AFIT. This mirror uses the same concept as the bimorph mirror only with one layer of piezoelectric material. The out-of-plane motion is achieved because the piezoelectric material is bonded to a silicon substrate, which does not move with applied voltage. Thus, the voltage creates bending with just one layer of piezo-electric material. This technique is also being used at the Jet Propulsion Laboratory, shown in Figure 6.

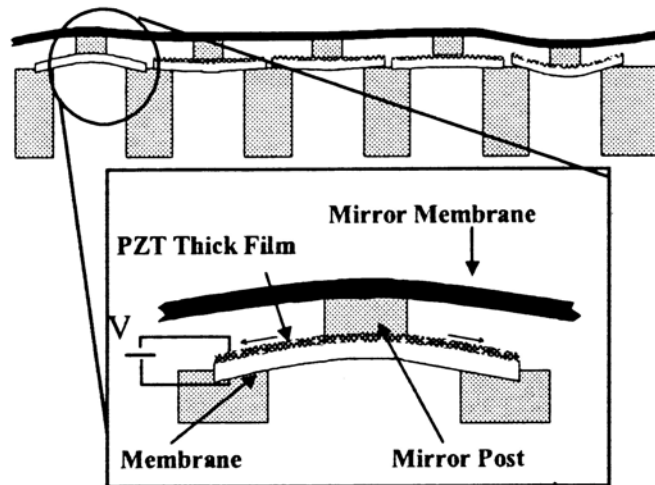


Figure 6: Design of a Unimorph System (21)

The design used by the Jet Propulsion Laboratory has the inherent disadvantage of the rigid support structure, as shown in Figure 6. This would cause the mirror to have a much higher areal density.

Another design for actuation of deformable mirrors is a membrane bonded to electrostatic actuators embedded in a dielectric substrate. These electrostatic actuators expand and contract based on voltages applied through the dielectric substrate (18).

Two other interesting designs are the segmented mirror design and the liquid crystal design. The segmented mirror consists of a large number of small tip, tilt, and piston actuators arranged in a pattern to make up the entire mirror surface. These actuators are then individually controlled in order to control the surface of the mirror. The follow up to Hubble, the James Webb Space Telescope, uses this type of design. The liquid crystal design consists of a number of liquid crystal modules oriented in such a way that the phase of light passing through them can be controlled via applied electric fields. This design does not modify the mirror surface at all but merely modifies the phase of the incident electro-magnetic field (18).

These are just a few of the various methods of actuating membrane mirrors. Research has been done in a number of areas including actuating the surface with an electron gun (10) as well as control of liquid based deformable mirrors through electrocapillary actuation (19). Many of these designs are not applicable to space applications. For instance, the methods that require a solid substrate are not applicable for large diameter mirrors because they cannot be folded for launch. Any methods that require exterior devices such as the electron gun to actuate the surface may not achieve the desired low areal densities due to the requirement for additional actuating equipment. The designs that apply well to space situations are the unimorph/bimorph design and the segmented mirror design. The unimorph/bimorph design is the focus of this research.

III. Development of Sensing Method

3.1 Overview

The primary focus of the research was to develop a new method of sensing the deformation of the mirror's surface. The method explored was to use a two-layer PVDF approach with one layer used for sensing and one layer used for actuation. The first step in this process was to fabricate a two-layer mirror. The testing of this mirror consisted of measuring the frequency response function in order to determine a state-space realization for the system, with the voltage on one layer for the input and the voltage on the other layer for the output. The goal was to use a state-space realization combined with a method to convert output voltage to Zernike coefficients in order to implement a control scheme. Figure 7 shows a diagram of a possible control system with the efforts of this research highlighted.

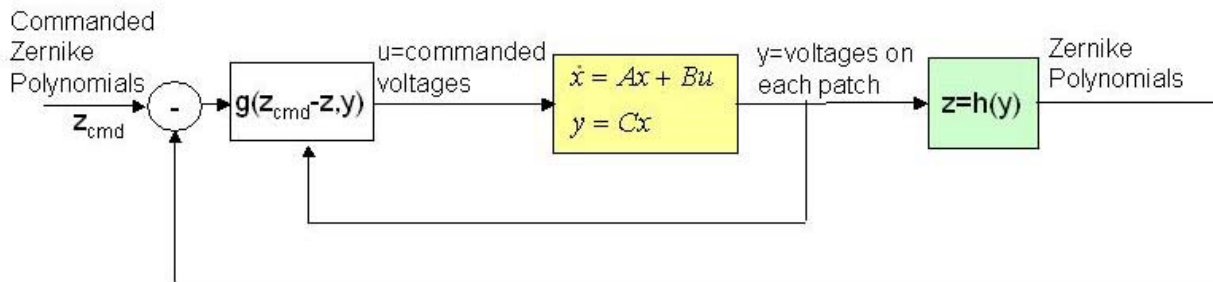


Figure 7: Possible Control System for Deformable Mirror

This control system assumes that the function 'z' is able to map the output voltages into the true Zernike Polynomial coefficients. This will only be the case if there are enough actuator/sensor pairs to accurately represent each Zernike Polynomial and if the equations of motion that govern the mirror as well as the equation that converts voltage to displacement are accurate. In the

following sections it is assumed that this is the case. The areas where this assumption breaks down are identified and discussed.

3.2 Theoretical Development

The frequency response function (FRF) is defined as the Fourier transform of the impulse response function. With the impulse response function it is possible to develop a model for the system that will give the correct representation of the input/output relationship. This is necessary in order to develop a valid control scheme. After a state-space realization is achieved it is necessary to convert the output voltages to displacements. To do this, one must solve the governing differential equation. Finally, once the displacements are obtained, they can be easily converted to Zernike polynomials. Figure 8 shows a diagram of the theoretical development of this research effort with the key equations highlighted. The full theoretical development is given in the following sections.

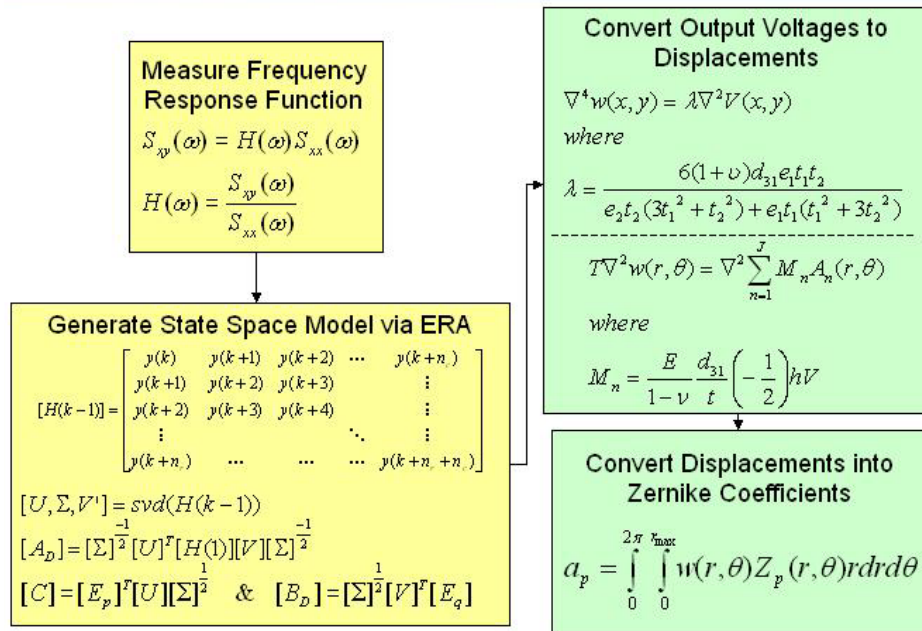


Figure 8: Flowchart Depicting Theoretical Development

3.2.1 FRF Development

Please note that the following derivation closely follows the notes given by Dr. Richard Cobb (2). Consider a system in which the output and the input can be measured, but the systems itself is unknown. The output of such a system to an arbitrary input would be given by the convolution of the impulse response function with the input to the system (Eq 1).

$$y(t) = \int_0^t h(\xi)x(t - \xi)d\xi \quad (1)$$

Also, the frequency response function (FRF) of the system is defined as the Fourier transform of the impulse response function, $h(t)$.

$$H(\omega) = \mathfrak{F}\{h(t)\} = \int_{-\infty}^{\infty} h(t)e^{-i\omega t} dt \quad (2)$$

The input autocorrelation is defined in terms of expected values as the following:

$$R_{xx}(\tau) = E[x(t) \quad x(t + \tau)] \quad (3)$$

And the cross-correlation between the output and the input of this system is defined as follows:

$$R_{xy}(\tau) = E[x(t) \quad y(t + \tau)] \quad (4)$$

These correlations are also defined in terms of the inverse Fourier transforms of the auto power spectral density, S_{xx} , and cross power spectral density, S_{yy} , respectively (see Eq 5).

$$\begin{aligned} S_{xx}(\omega) &= \mathfrak{F}\{R_{xx}(\tau)\} \\ S_{xy}(\omega) &= \mathfrak{F}\{R_{xy}(\tau)\} \end{aligned} \quad (5)$$

Now, returning to the linear system previously discussed, consider the response of the system to an input $x(t+\tau)$ and its corresponding cross-correlation.

$$y(t + \tau) = \int_{-\infty}^{\infty} h(\xi)x(t + \tau - \xi)d\xi$$

$$R_{xy}(\tau) = E \left[x(t) \int_{-\infty}^{\infty} h(\xi)x(t + \tau - \xi)d\xi \right] \quad (6)$$

Because $x(t)$ is not a function of ξ the expectation operator can be moved to the inside of the integral so that the cross-correlation can be written as the following:

$$R_{xy}(\tau) = \int_{-\infty}^{\infty} h(\xi)E[x(t) x(t + \tau - \xi)]d\xi \quad (7)$$

Now, substituting the previous value given for the autocorrelation, the cross-correlation can be written as the convolution of the impulse response function and the autocorrelation.

$$R_{xy}(\tau) = \int_{-\infty}^{\infty} h(\xi)R_{xx}(\tau - \xi)d\xi \quad (8)$$

Finally, use the property of Fourier transforms which states the convolution of signals in the time domain is equal to multiplication of signals in the frequency domain. This reduces Equation 8 to a multiplication of the FRF and the auto power spectral density. So the FRF can be written as the ratio of the cross power spectral density to the auto power spectral density (see Eq 9).

$$S_{xy}(\omega) = H(\omega)S_{xx}(\omega)$$

$$H(\omega) = \frac{S_{xy}(\omega)}{S_{xx}(\omega)} \quad (9)$$

By applying this to the system in question (deformable mirror), one can see that this will give a transfer function that will relate voltage put into the system (via the acoustic source or the patches) to the voltage measured on each of the patches.

3.2.2 State Space Realization

The next step is to convert this transfer function into a state space realization. This can be done as well by closely following notes given by Cobb (2). The method used is called Eigensystem Realization Algorithm (ERA). A discrete representation of a state space system yields the following output for a discrete pulse input (i.e. $f=[1,0,0,0,\dots]$)

$$\begin{aligned} y(k) &= [C] \{B_D\}_{col\ of\ B}, k = 0 \\ y(k) &= [C][A_D]^{k-1}[B_D] \end{aligned} \quad (10)$$

where C , B_D , and A_D are the discrete representations of the state space matrices. Now define the Hankel matrix as follows:

$$[H(k-1)] = \begin{bmatrix} y(k) & y(k+1) & y(k+2) & \cdots & y(k+n_c) \\ y(k+1) & y(k+2) & y(k+3) & & \vdots \\ y(k+2) & y(k+3) & y(k+4) & & \vdots \\ \vdots & & & \ddots & \vdots \\ y(k+n_r) & \cdots & \cdots & \cdots & y(k+n_r+n_c) \end{bmatrix} \quad (11)$$

The variables n_r and n_c are arbitrary integers that satisfy the following relationships:

$$\begin{aligned} pn_r &\geq 2N \\ qn_c &\geq 2N \\ \text{where} & \\ p &= \# \text{ outputs}, q = \# \text{ inputs}, N = \# \text{ peaks} \end{aligned} \quad (12)$$

By substituting the previous definition of $y(k)$ into Equation 11 the result shown in Equation 13 is obtained.

$$[H(k)] = [Q][A_D]^k [W]$$

where

$$[Q] = \begin{bmatrix} C \\ CA_D \\ \vdots \\ CA_D^{n_r-1} \end{bmatrix} \quad (13)$$

$$[W] = \begin{bmatrix} B_D & A_D B_D & \cdots & A_D^{n_c-1} B_D \end{bmatrix}$$

$[H(k)]$ is a known quantity populated by finding $y(k)$, which is the inverse Fourier transform of the FRF calculated in the previous section. The unknowns are the three state space matrices.

The algorithm used calculates these matrices from the Hankel matrix. Recalling Equation 13, the Hankel matrix for $k=0$ can be written as $[H(0)]=[Q][W]$ since an exponent of zero on the center matrix turns it to the identity matrix. Now, singular value decomposition (SVD) is used on $H(0)$ in order to turn it into a product of three matrices.

$$[H(0)] = [Q][W] = [U][\Sigma][V]^T = [U][\Sigma]^{\frac{1}{2}}[\Sigma]^{\frac{1}{2}}[V]^T \quad (14)$$

$$\therefore [Q] = [U][\Sigma]^{\frac{1}{2}}, [W] = [\Sigma]^{\frac{1}{2}}[V]^T$$

Note that $[\Sigma]$ is a diagonal matrix and $[U]$ and $[V]$ are unitary matrices. Therefore the same approach can be used with $[H(1)]$ to solve for $[A_D]$.

$$[H(1)] = [Q][A_D][W] = [U][\Sigma]^{\frac{1}{2}}[A_D][\Sigma]^{\frac{1}{2}}[V]^T \quad (15)$$

$$[A_D] = [\Sigma]^{\frac{-1}{2}}[U]^T [H(1)][V][\Sigma]^{\frac{-1}{2}}$$

Going back to equation 10, $y(1)$ is defined as $[C][B_D]$ for $k=1$. Equation 16 shows another representation for $y(1)$, which leads to a method for solving for $[C]$ and $[B_D]$.

$$y(1) = \begin{bmatrix} I_p & 0 & 0 & \dots \end{bmatrix} \begin{bmatrix} y(1) & y(2) & y(3) & \dots \\ y(2) & y(3) & y(4) & \dots \\ y(3) & y(4) & y(5) & \dots \\ \vdots & \vdots & \vdots & \ddots \end{bmatrix} \begin{bmatrix} I_q \\ 0 \\ 0 \\ \vdots \end{bmatrix} = [E_p]^T [H(0)] [E_q] \quad (16)$$

In this equation, $[I_p]$ is defined as an identity matrix with the number of outputs as the number of columns and rows and $[I_q]$ is defined as an identity matrix with the number of inputs as the number of columns and rows. Now, $[B_D]$ and $[C]$ can be found through Equation 17.

$$\begin{aligned} y(1) &= [C][B_D] = [E_p]^T [H(0)] [E_q] = [E_p]^T [U][\Sigma]^{\frac{1}{2}} [\Sigma]^{\frac{1}{2}} [V]^T [E_q] \\ \therefore [C] &= [E_p]^T [U][\Sigma]^{\frac{1}{2}} \quad \& \quad [B_D] = [\Sigma]^{\frac{1}{2}} [V]^T [E_q] \end{aligned} \quad (17)$$

Keep in mind that these state space matrices are for the discrete system. They will need to be converted back to the continuous domain through the use of a discrete to continuous converter such as the one available in Matlab.

3.2.3 Determining Zernike Shapes from Output Voltage

The state space realization given in the previous section gives an output of voltage on each of the patches. This output will be based on the movement of the mirror for the open loop case or a combination of the mirror's movement and the deformation caused by the input signals for the closed loop case. In some instances it may be desirable to report the output, not in voltages, but in some kind of mode-shape of the mirror itself. This allows for the control system to command a certain mode shape and have the mirror conform to that shape. For this research, the mode-shapes that were chosen are the Zernike polynomials. These are a basis set of orthogonal functions often used in the field of optics to describe the phase of a wave-front. The process to convert the voltage read by the sensor to Zernike coefficients is to solve the

differential equation governing the surface of the mirror to get displacement from voltage, and then to convert this displacement to Zernike coefficients.

During the course of this research it was discovered that two different equations are given for the displacement of the surface of the mirror due to voltage across the PVDF material. The first of these is given by Ellis (3) and alternatively by Vdovin, Loktev and Simonov (18) as the following:

$$\nabla^4 w(x, y) = \lambda \nabla^2 V(x, y)$$

where

$$\lambda = \frac{6(1+\nu)d_{31}e_1t_1t_2}{e_2t_2(3t_1^2 + t_2^2) + e_1t_1(t_1^2 + 3t_2^2)} \quad (18)$$

This equation is commonly known as the bi-harmonic equation and is the static equation that governs the motion of a plate. The values in the constant, λ , are defined in terms of the physical properties of the material in use. Table 1 defines the variables used in this constant and what physical properties they represent.

Table 1: Physical Properties of Material (10)

Variable	Physical Property	Value
ν	Poisson's Ratio	0.3
d_{31}	Piezoelectric constant of material	23e-12 (m/m)/(V/m)
e_1	Young's modulus of PVDF layer	4000e6 N/m ²
e_2	Young's modulus of substrate layer	1.013e6 N/m ²
t_1	Thickness of PVDF layer	52e-6 m
t_2	Thickness of substrate layer	0.0015 m

Because the material in question is non-isotropic, the Piezoelectric constant in one Cartesian direction (d_{31}) is not equal to the Piezoelectric constant in the other Cartesian direction (d_{32}). However, for the purpose of this analysis, these two values were assumed to be the same.

The second of these equations is given by Shepherd (12) and is reproduced in Equation 19.

$$T\nabla^2 w(r, \theta) = \frac{E}{1-\nu} \frac{d_{31}}{t} \left(\frac{-h}{2} \right) \sum_{i=1}^J V_i F_i(r, \theta) \quad (19)$$

This equation is referred to as the membrane equation and it gives the static results for a membrane under tension.

Because of the discrepancies between these two equations the focus of this research was shifted to determining which of the two equations best fit the experimental data. The method that was utilized was to do a modal analysis of the dynamic versions of these equations and compare to the experimental data. The predicted natural frequencies of the mirror can be found using the homogenous differential equation. For the plate equation this is given as the following,

$$C_1 \nabla^4 w(r, \theta, t) - C_2 w^{(4)}(r, \theta, t) = 0 \quad (20)$$

where C_1 and C_2 are arbitrary constants that can be solved for by applying the boundary conditions and the '(4)' superscript refers to the fourth time derivative. In order to solve for the natural frequencies, assume separation of variables.

$$w(r, \theta, t) = W(r, \theta) e^{j\omega_n t} \quad (21)$$

Substitute this value into equation 20 and solve for the differential equation in terms of r and θ only.

$$C_1 e^{j\omega_n t} \nabla^4 W(r, \theta) - C_2 \omega_n^4 e^{j\omega_n t} W(r, \theta) = 0 \quad (22)$$

$$e^{j\omega_n t} \left(\nabla^4 W(r, \theta) - \frac{C_2}{C_1} \omega_n^4 W(r, \theta) \right) = 0 \quad (23)$$

$$\begin{aligned} \nabla^4 W(r, \theta) - \lambda W(r, \theta) &= 0 \\ \lambda &= \frac{C_2}{C_1} \omega_n^4 \end{aligned} \quad (24)$$

Equation 24 has an eigenvalue solution (with zero boundary conditions) given by Polyanin (12).

This can be written in terms of the zeros of the Bessel functions of the first kind and the modified Bessel functions of the first kind.

$$\lambda_{mn} = \frac{\beta_{mn}^4}{R^4} \quad (25)$$

$$\text{where, } J_n(\beta)I_n'(\beta) - I_n(\beta)J_n'(\beta) = 0$$

In this equation the ‘J’ function is the Bessel function of the first kind and the ‘I’ function is the modified Bessel function of the first kind. The ‘R’ in equation 25 is the radius of the mirror.

Recall, from equation 24, lambda is a function of the natural frequency. Using this, one can solve for natural frequency in terms of β .

$$\frac{C_2}{C_1} \omega_n^4 = \frac{\beta_{mn}^4}{R^4} \quad (26)$$

$$\omega_{mn} = \sqrt[4]{\frac{C_1}{C_2} \frac{\beta_{mn}^4}{R^4}} = k\beta_{mn} \quad (27)$$

Table 2 gives numerical values for beta.

Table 2: Numerical Values of Beta

m\n	1	2	3	4
0	3.196	6.306	9.439	12.58
1	4.611	7.799	10.96	14.11
2	5.906	9.197	12.40	15.58
3	7.144	10.54	13.79	17.01

The method used to predict the values of ω_{mn} was to set the first measured value equal to the first predicted frequency in order to find the constant ‘k’. This value was then used to calculate all the other frequencies.

$$\omega_{01_{meas}} = k\beta_{01}$$

$$k = \frac{\omega_{01_{meas}}}{\beta_{01}} \quad (28)$$

By using this method all of the predicted natural frequencies corresponding to the values of beta can be calculated. These are given in Table 3.

Table 3: Predicted Natural Frequencies from Plate Equation (Hz)

m\n	1	2	3	4
0	76	149.95	224.46	299.15
1	109.65	185.46	260.67	335.53
2	140.44	218.70	294.87	370.49
3	169.88	250.64	327.92	404.49

In addition to the natural frequencies, equation 24 can be used to predict the vibrational mode shapes corresponding to those natural frequencies. Polyanin (12) gives the solutions to the mode shapes as the following in terms of a sine component and a cosine component.

$$\begin{aligned}
 W_{mn}^{(c)}(r, \theta) &= \left[I_m(\beta_{mn}) J_m\left(\beta_{mn} \frac{r}{R}\right) - J_m(\beta_{mn}) I_m\left(\beta_{mn} \frac{r}{R}\right) \right] \cos(m\theta) \\
 W_{mn}^{(s)}(r, \theta) &= \left[I_m(\beta_{mn}) J_m\left(\beta_{mn} \frac{r}{R}\right) - J_m(\beta_{mn}) I_m\left(\beta_{mn} \frac{r}{R}\right) \right] \sin(m\theta)
 \end{aligned} \tag{29}$$

The solution for the full mode shape can be found by adding these two together. This has been done for the values of beta given previously and the results are displayed below.

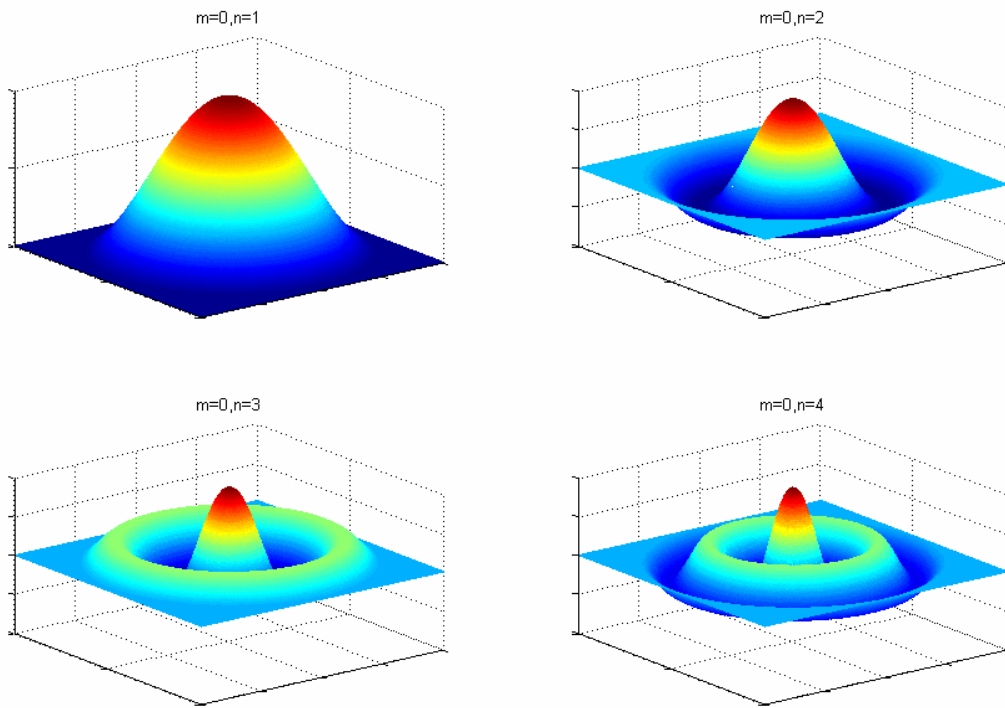


Figure 9: Mode Shapes from Plate Equation ($m=0$)

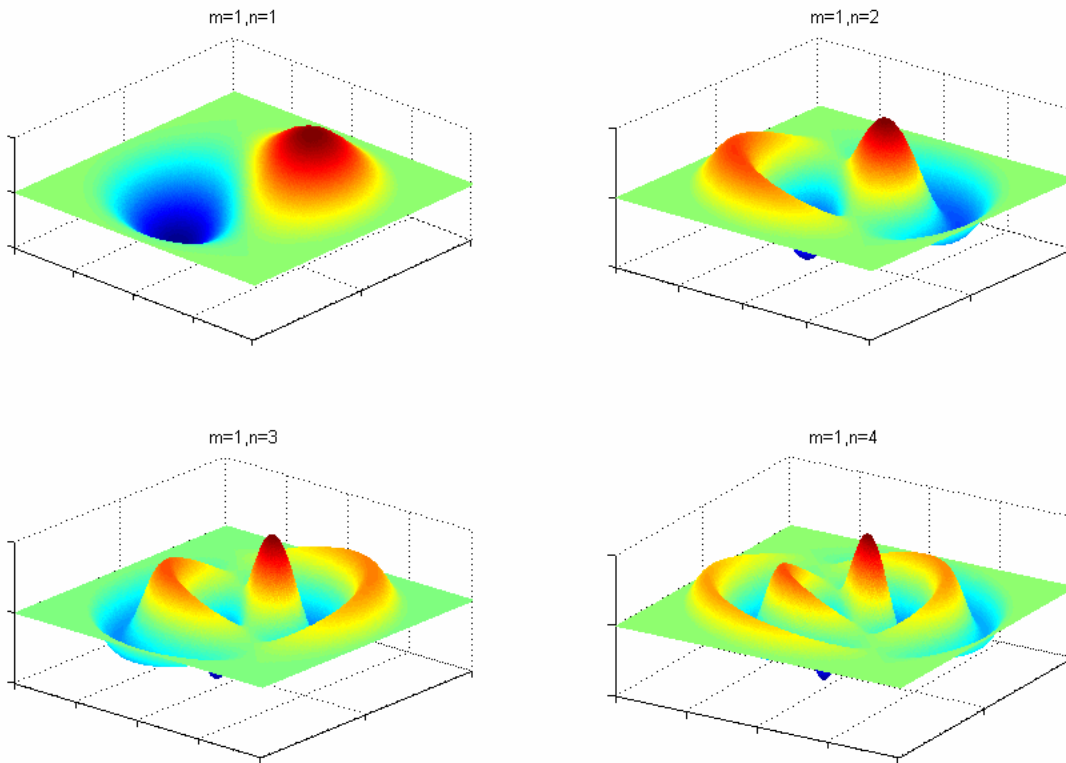


Figure 10: Mode Shapes from Plate Equation ($m=1$)

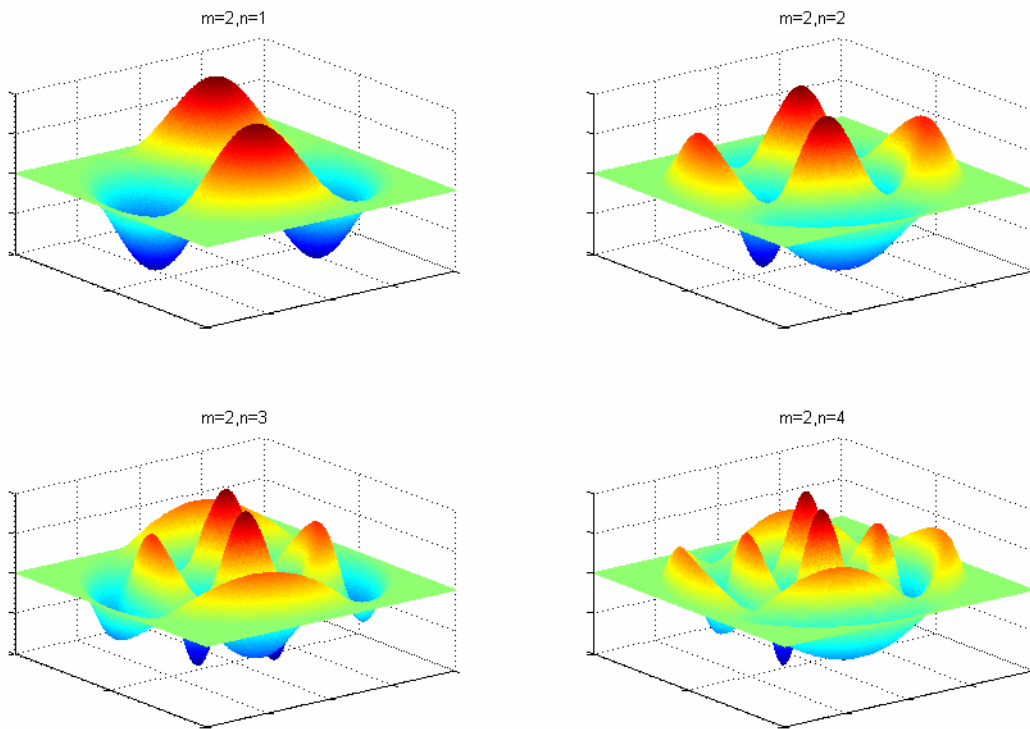


Figure 11: Mode Shapes from Plate Equation ($m=2$)

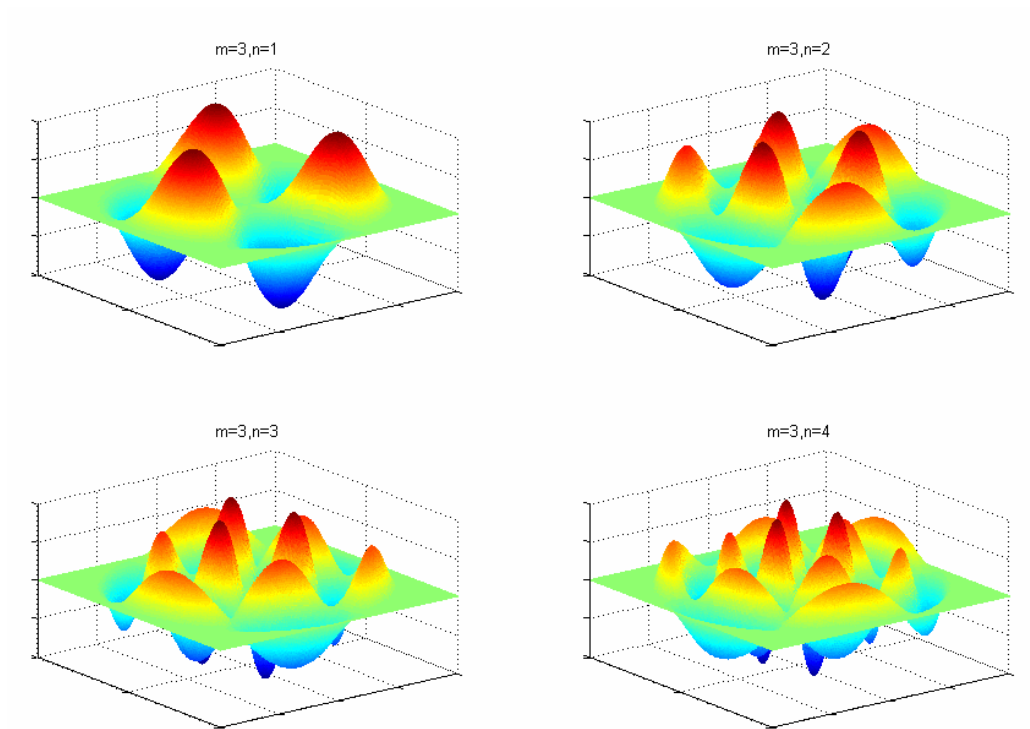


Figure 12: Mode Shapes from Plate Equation ($m=3$)

The method for predicting natural frequencies and vibrational mode shapes from the membrane equation is very similar to the previous method. It is also outlined in Trad (17) and so will not be covered in detail here. The predicted natural frequencies are given in Table 4.

Table 4: Predicted Natural Frequencies from Membrane Equation

m\n	1	2	3	4
0	76	174.45	273.50	372.64
1	121.10	221.71	321.50	421.09
2	162.30	266.01	367.23	467.61
3	201.63	308.48	411.32	512.74

The predicted vibrational mode shapes are given in Figure 13 through Figure 16.

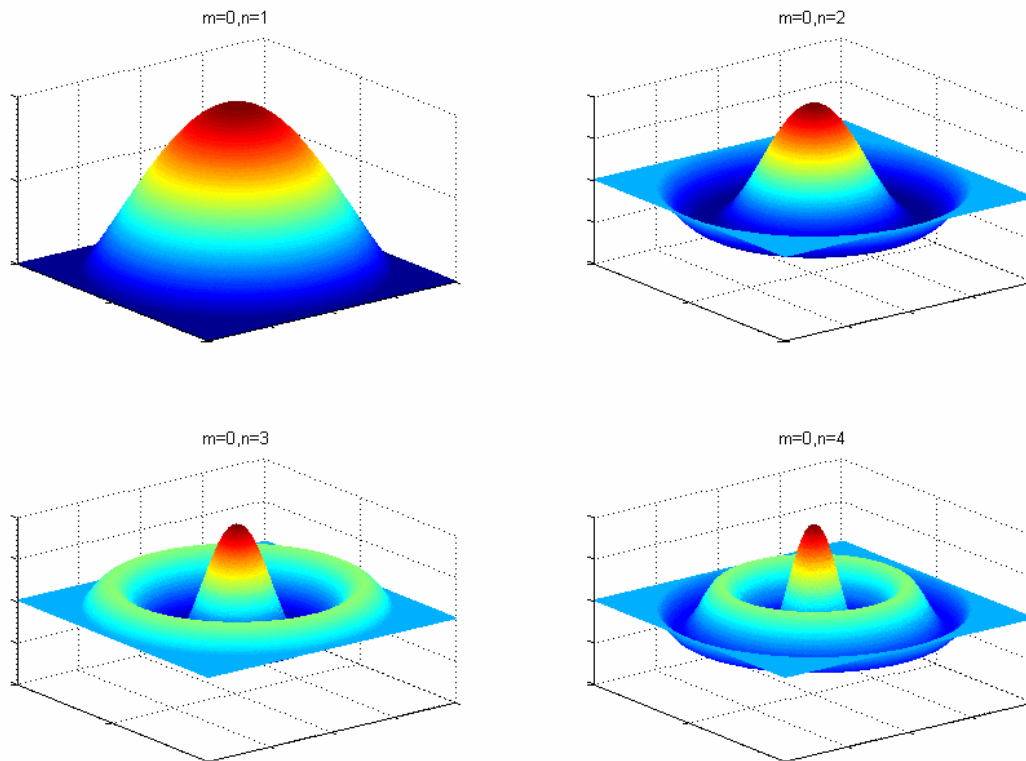


Figure 13: Mode Shapes from Membrane Equation ($m=0$)

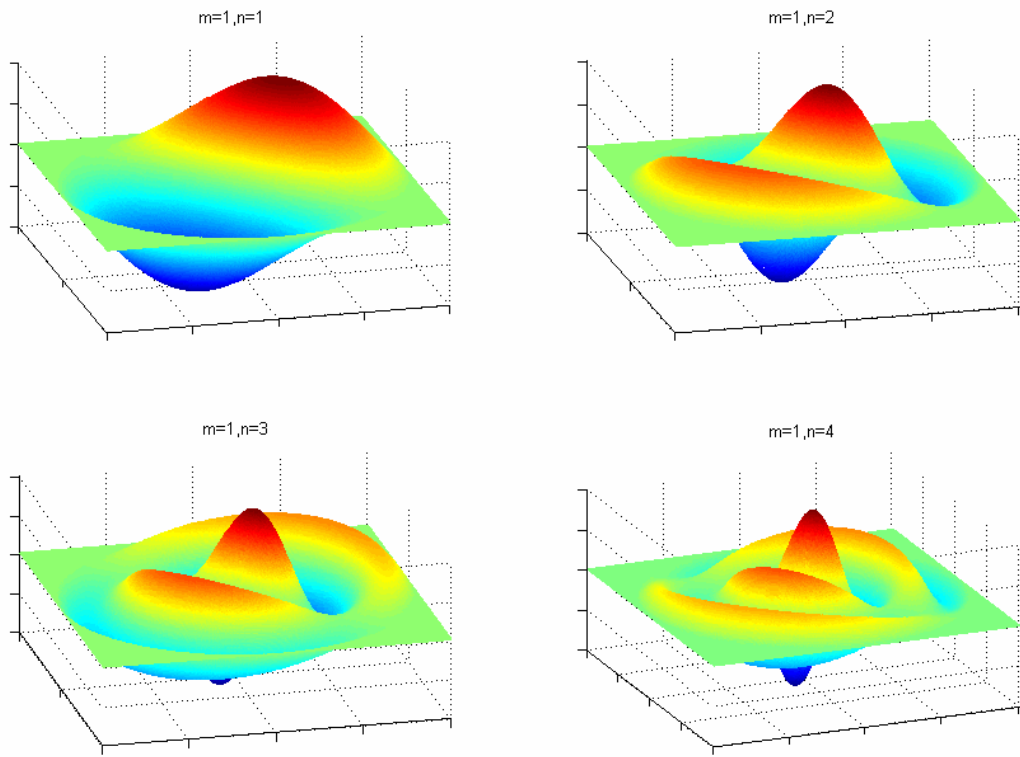


Figure 14: Mode Shapes from Membrane Equation ($m=1$)

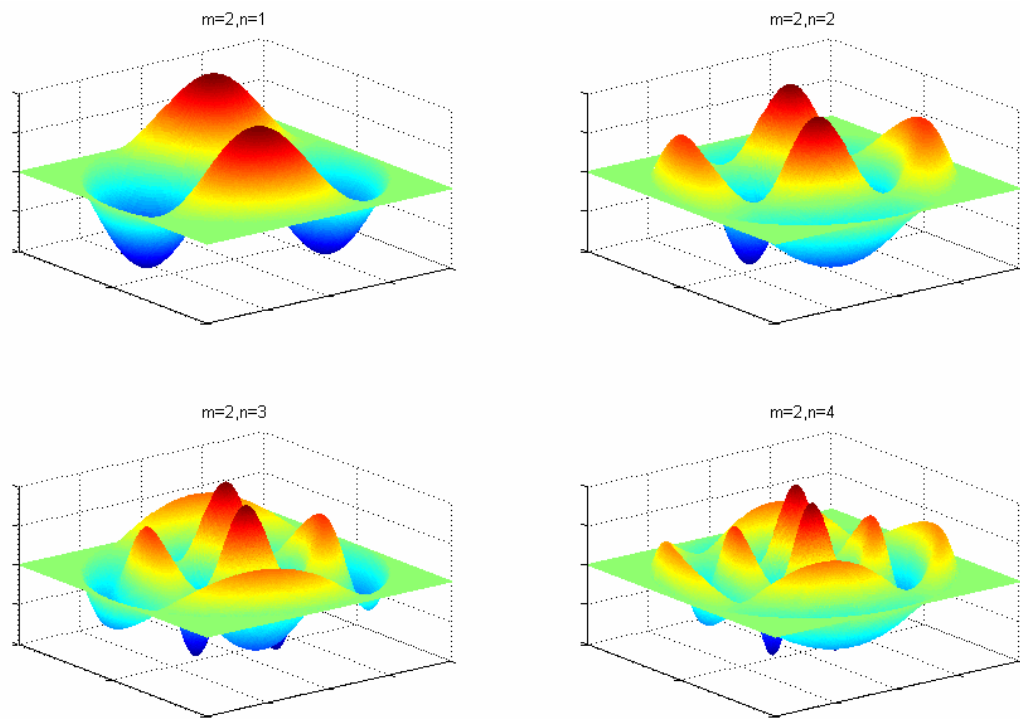


Figure 15: Mode Shapes from Membrane Equation ($m=2$)

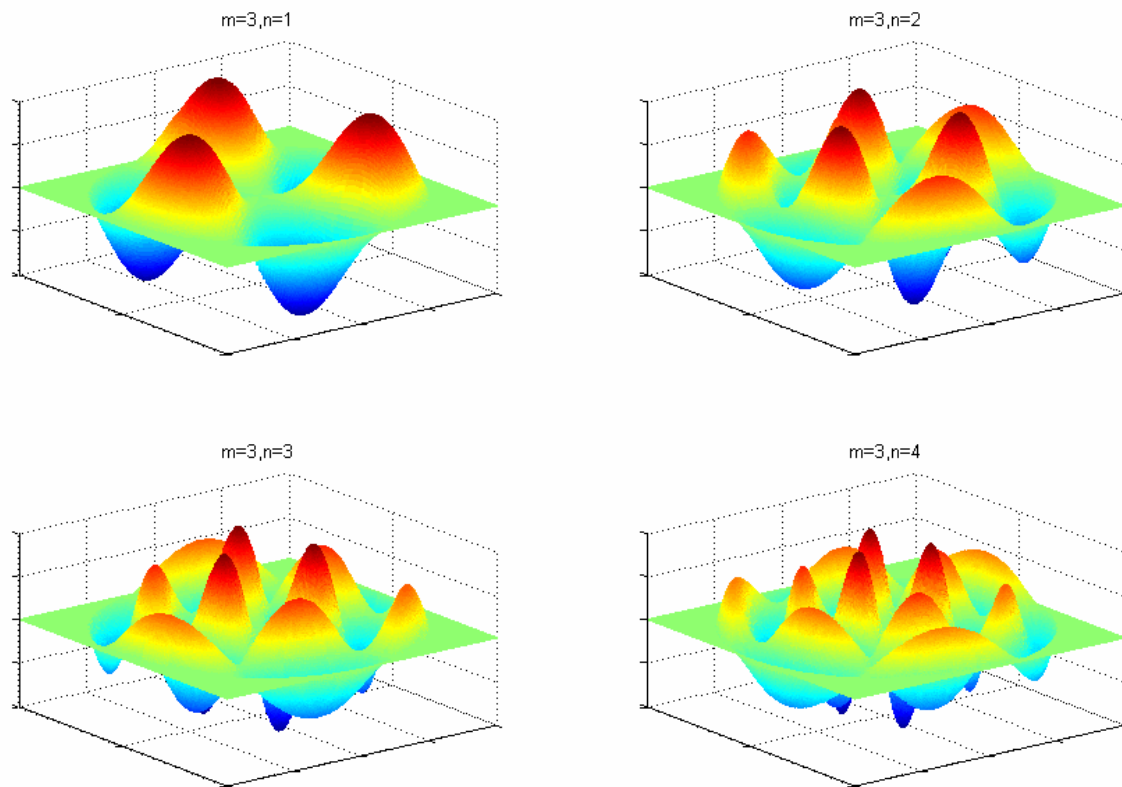


Figure 16: Mode Shapes from Membrane Equation ($m=3$)

3.3 Fabrication

Fabrication for the two-layer mirror followed closely with the process outlined by Trad (17). First, two 14 in long pieces of PVDF material were cut. The positive side and the one¹ direction were marked on each of these pieces. The 7-electrode pattern was then drawn by hand onto the positive surface of each of the two pieces. Great care was taken to ensure that the pattern was in the same location and orientation between the two sheets of material. First, the center of one sheet was found. The pattern stencil was taped down so that its center lined up

¹ The one direction of the material refers to the direction in which the fibers in the material lie.

with the center of the PVDF piece. Next, the edges of the pattern stencil were marked with a permanent marker. The distance from the edge of the pattern stencil to the edge of the PVDF material was measured and recorded. After the pattern was drawn onto the PVDF material, the pattern stencil was removed and the previously recorded dimensions were used to mark the place where the pattern stencil was to be taped to the second piece of PVDF material. The pattern was then drawn onto the second piece of material.

The next step in the process was to etch the pattern onto the material using ferric chloride. This was applied with a cotton ball for large areas and with a cotton swab for more detailed work. The area over the entire pattern was coated with the ferric chloride, and then it was washed with water. At this point, one of the pieces was chosen to be the sensor and one was chosen to be the actuator. The sensor was marked with a small "s" in the corner in order to distinguish it. The pieces were then turned over to the negative side and ferric chloride was applied to the entire surface of the actuator piece. This resulted in a transparent piece of PVDF with only the pattern visible. The area on the small rectangular portion of the leads of the sensor piece was also etched with the ferric chloride. This allows a window so that the two layers will be able to be lined up correctly in the tensioning phase.

The final step in the process was to tension the PVDF and to mount it to an aluminum ring. This was also done similar to the process outlined in Trad (17). The sensor piece was placed in the tensioning ring first with the pattern facing downward, and the clamps were tightened two at a time using opposite corners together. The clamps were turned an approximately 45 degrees each time until none of the clamps could turn any more. It is important that the tension on this piece of PVDF and the second piece of PVDF is the same. Therefore, a more accurate method of determining the tension applied to the PVDF needs to be

identified. After the PVDF was tensioned, the aluminum ring was glued into place using M-bond 610 epoxy. The epoxy was given 72 hours to cure, and then the ring and PVDF were removed from the tensioning apparatus. The excess PVDF material was trimmed away so that only the leads remained outside of the aluminum ring. Finally, the actuator piece was put into the tensioning ring. The copper colored pattern was on the top and was clearly visible. The PVDF was tightened in the same manner as before taking great care to apply the same amount of tension. The surface of the PVDF was brushed with the epoxy and the aluminum ring with the sensor sheet was placed on the actuator sheet. The leads of the sensor sheet were lined up carefully with the leads of the actuator sheet by looking through the "windows" that were previously etched. This had to be done quickly because the epoxy tended to dry quickly. This setup was then given 72 hours to cure. After the curing process was done, the finished mirror was removed from the tensioning apparatus and the excess PVDF material was trimmed from the actuator layer.

The mirror would normally be coated with a silicon substrate as was outlined in Trad (17). This was not done in order to save time. However, it was later determined the layer of silicon was required for out-of-plane motion. In a unimorph design, the out-of-plane motion is a result of the PVDF layer being offset from the neutral axis of the mirror. The silicon layer establishes the neutral axis and is therefore required for out-of-plane motion. Because of this the mirror constructed by Trad (17) labeled 7-patchA was used for the laser vibrometer test.

3.4 Testing

3.4.1 Test Overview

The testing of the 7-patch two-layer mirror consisted of actuation with all seven of the patches individually. The first test measured the surface displacement using a scanning laser vibrometer. The objective of this test was to determine which of the two previously mentioned equations corresponded best to the experimental data. The purpose of the patch input test was to determine the frequency response function (FRF) for the mirror surface based on the voltage applied across the patches. The final objective was to develop a state-space model of the system relating voltage across the input patches to voltage out of the patches.

3.4.2 Laser Vibrometer test

The laser vibrometer test consisted of actuating the patches with a voltage source and measuring the surface deflection with a scanning laser vibrometer. The mirror was placed on two steel bars suspended by the tensioning ring as shown in Figure 17.



Figure 17: Test Setup for Laser Vibrometer Test

The scanning laser vibrometer was then pointed down at the mirror. A pattern was created that outlined one of the patches. This pattern was then rotated around for successive test so that the FRF for each of the patches, with voltage across one of the patches as the input, was calculated. The results of this test are discussed in section 3.5.

3.4.3 Patch Output

The patch input test was conducted in the same manner as the laser vibrometer test except that the measured output was taken from the patches. This test used a computer equipped with SignalCalc. This is a software program that can generate a signal for an input and accept multiple output signals. It can then calculate FRF's based on these signals. The signal generator

from the SignalCalc computer was connected to patch one for the first test. Figure 18 shows a diagram of the 7-patch mirror configuration.

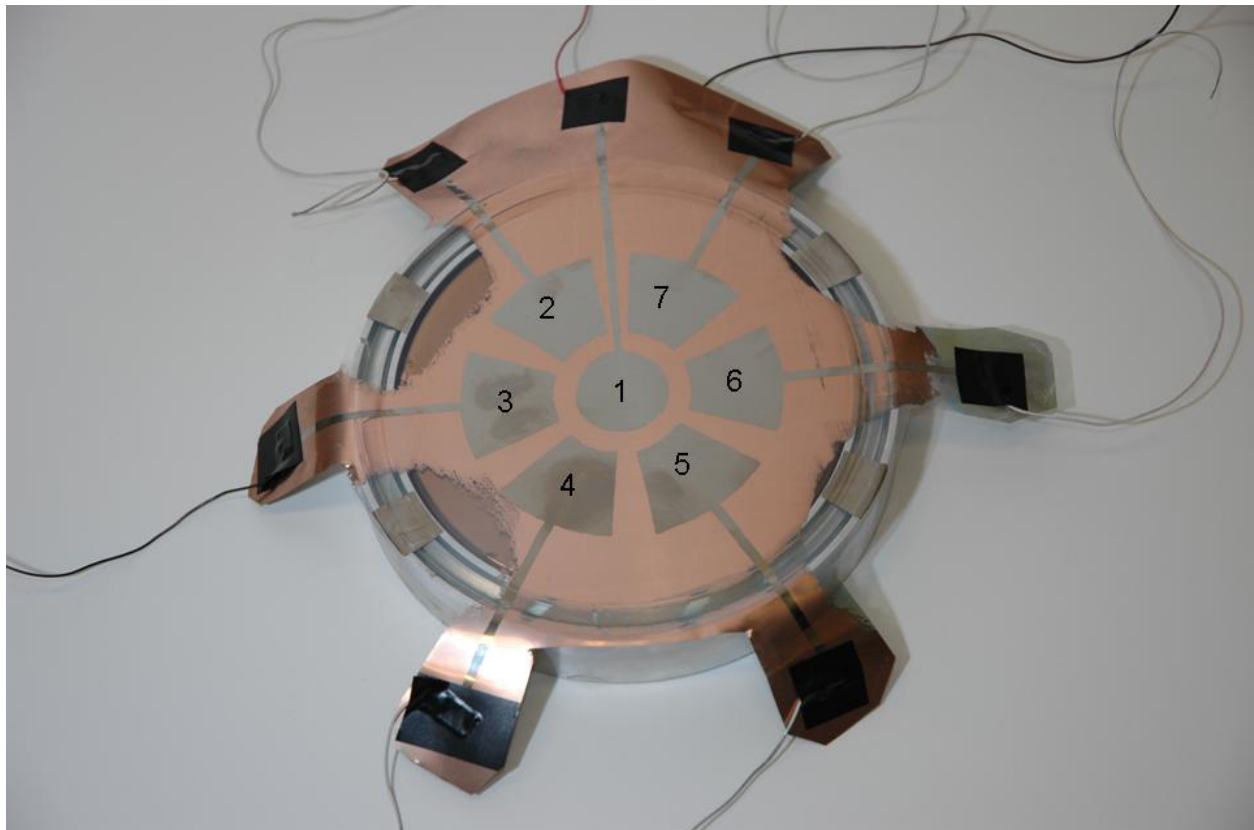


Figure 18: Layout of 7-Patch Mirror Showing Location of Each Patch

The input signal was then moved to each of the different patches successively so that an FRF for each input could be generated. The results from these tests were not what was expected and are discussed in the following section. Because of this the final step of developing a state-space model was not completed.

3.5 Results

3.5.1 Results Overview

With each of the tests previously described, an FRF relating input to each of the patches as output was obtained. The results from the laser vibrometer test proved very successful and were useful in comparing the experimental value with the predicted values from the two equations. The patch output test did not turn out as expected. Some possible reasons for this are discussed. The conclusions drawn from these tests are discussed in Chapter six.

3.5.2 Discussion of Results

The laser vibrometer was able to measure the FRF of each of the patches with respect to a single patch input. One of these FRF's is shown below.

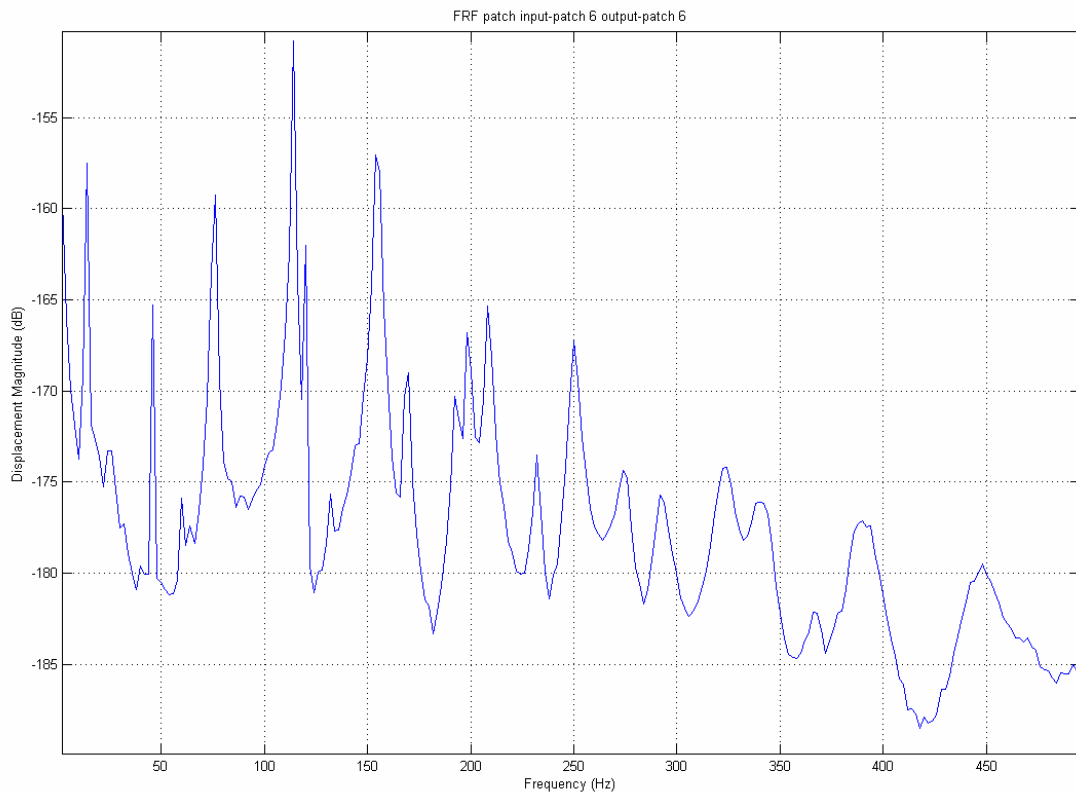


Figure 19: FRF, Patch 6 input, Patch 6 output

The measured natural frequencies are given in Table 5.

Table 5: Measured Natural Frequencies (Hz)

m\n	1	2	3	4
0	76	120	170	208
1	88	132	192	N/A
2	114	154	198	N/A

These values were then compared to the predicted values given earlier. The percent difference between the values is given in Table 6 for the plate equation and in Table 7 for the membrane equation.

Table 6: Percent Difference Between Measured and Predicted Frequencies (plate equation)

m\n	1	2	3	4
0	0	22.19	27.61	35.95
1	21.91	33.68	30.32	N/A
2	20.78	34.72	39.31	N/A

Table 7: Percent Difference Between Measured and Predicted Frequencies (membrane equation)

m\n	1	2	3	4
0	0	36.99	46.67	56.71
1	31.66	50.72	50.44	N/A
2	34.96	53.34	59.88	N/A

As can be seen from the previous tables the plate equation predicts the natural frequencies more accurately than the membrane equation. The vibrational mode shapes were also compared to the experimental mode shapes. The experimental mode shapes were determined by actuating the mirror with an acoustic source and measuring the displacement of a grid of points with the laser vibrometer. The grid that was set up has 36 angular grid points and 8 radial grid points for each angular point. The individual displacement for each of these points was measured and the results were read into Matlab. Matlab was then used to interpolate the results so that the experimental

grid and the theoretical grid matched each other. The data was then normalized by dividing the entire grid by the maximum value in the grid. The theoretical mode shapes calculated earlier were normalized and subtracted from the normalized experimental result. The results from two of these comparisons are given below.

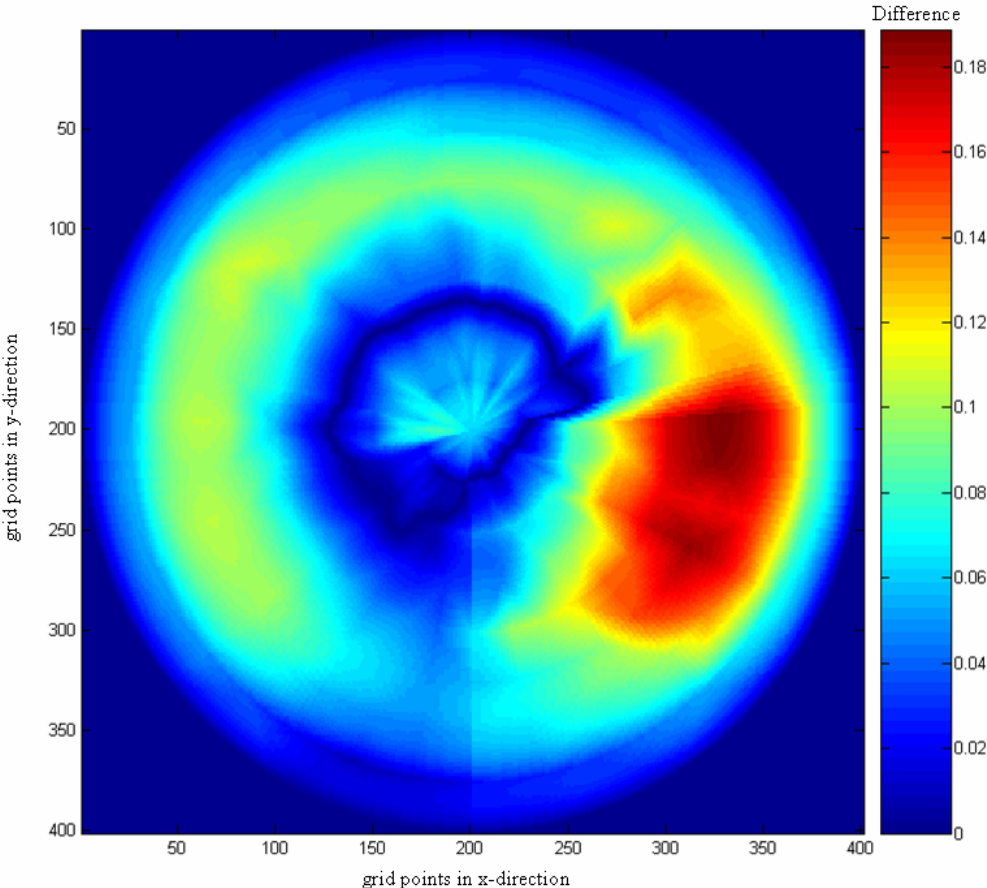


Figure 20: Difference Between Predicted Shape and Experimental Shape (plate equation, $m=0$, $n=1$)

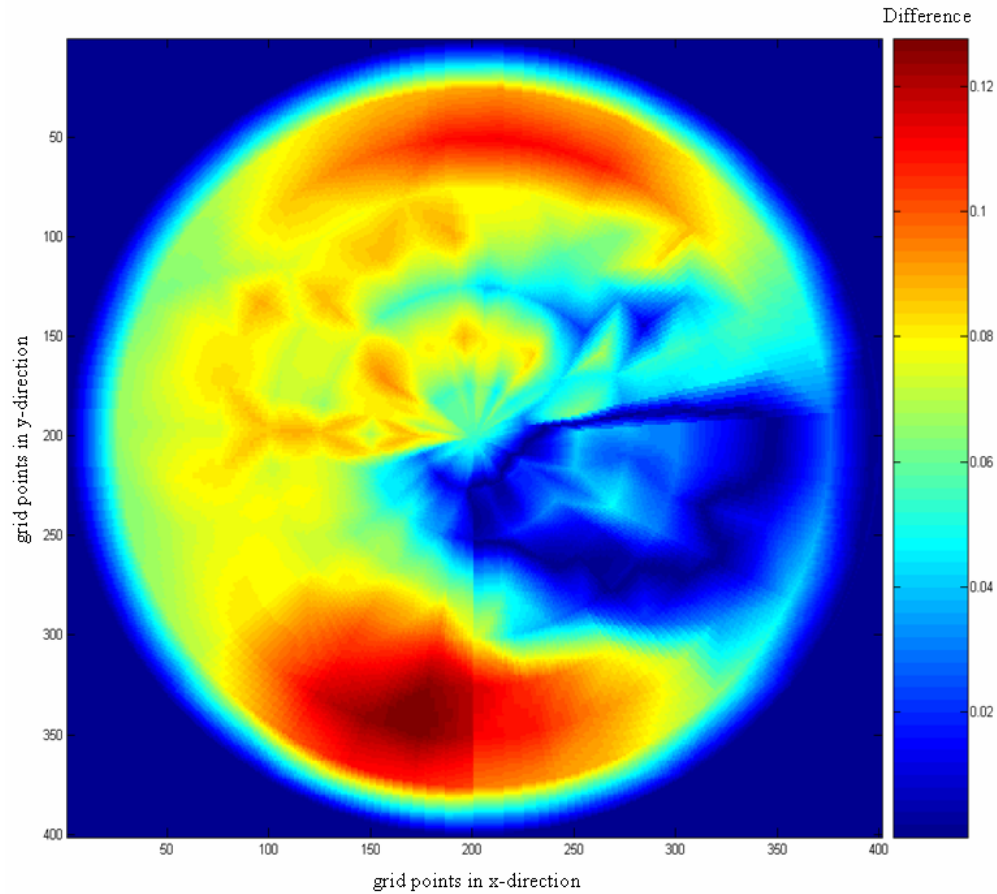


Figure 21: Difference Between Predicted Shape and Experimental Shape (membrane equation, $m=0$, $n=1$)

The average difference for the plate equation, when compared to experimental data, is equal to 0.052 and the average difference for the membrane equation is 0.046. This average value was calculated by simply adding up the difference over all of the points and dividing by the total number of points. The same procedure was done for the $m=2$, $n=1$ mode and the results are presented below.

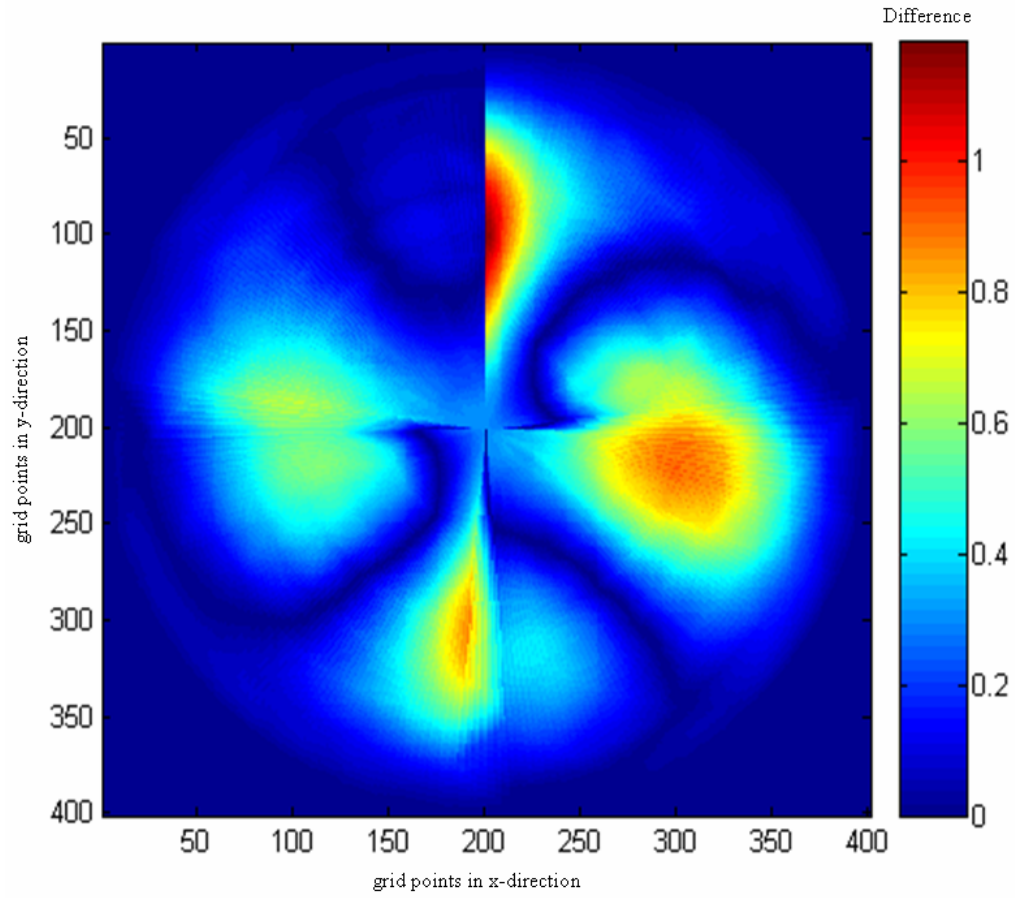


Figure 22: Difference Between Predicted Shape and Experimental Shape (plate equation, $m=2$, $n=1$)

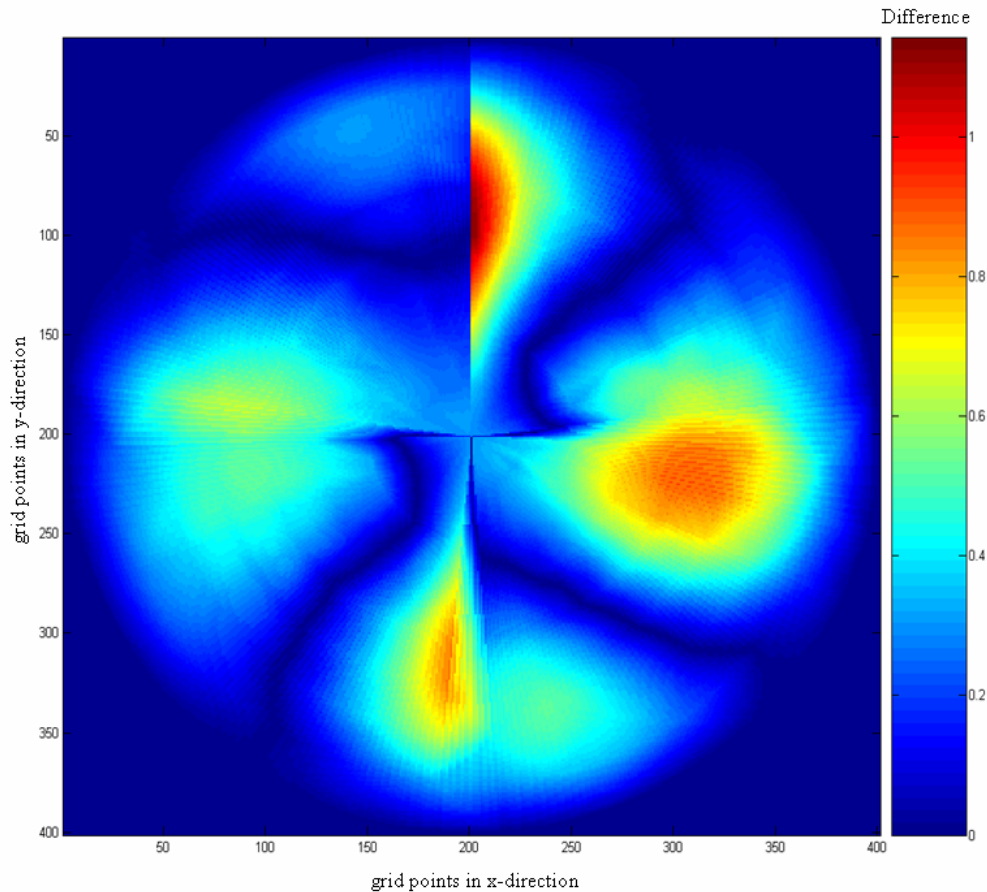


Figure 23: Difference Between Predicted Shape and Experimental Shape (membrane equation, $m=2$, $n=1$)

The predicted mode shapes shown above differed in phase from the experimental shape. This accounts for the areas in the plots where the difference gets large. The lines that are visible in the previous figures as well as the figures for the $m=0, n=1$ mode are a consequence of the conversion from polar coordinates to Cartesian coordinates. These are not actually in the data. Overall, the average difference for the plate equation is 0.185 and the average difference for the membrane equation is 0.216. These values show that the both predicted mode shapes are close to the experimental mode shape. However, the prediction for the natural frequencies is much better for the plate equation than the membrane equation. The actual equation governing the dynamics of the mirror is likely some combination of both of these equations.

The patch output test yielded far worse results. Figure 24 shows a typical result for the FRF relating the voltage into a patch with the voltage out of a patch.

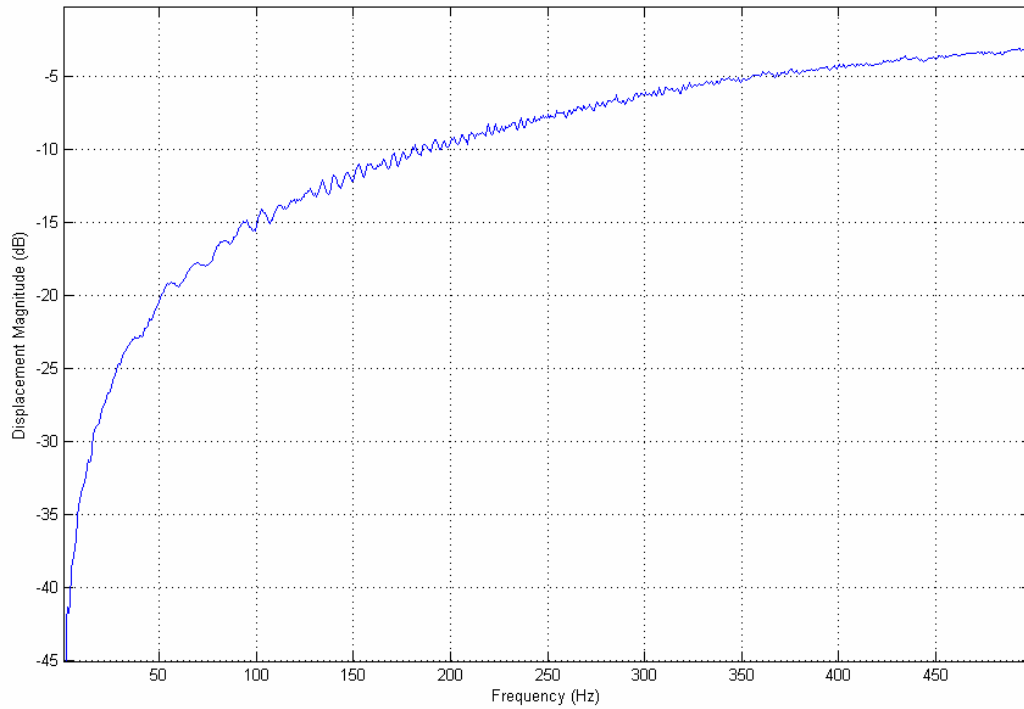


Figure 24: FRF Result From Patch Output Test

It was determined that the primary reason for the discrepancies in this plot is due to the voltage dissipation. The voltage created from a strain in the PVDF material dissipates very rapidly and therefore the voltage response does not track well with a sine wave at low frequencies. This is shown in Figure 25 and Figure 26.

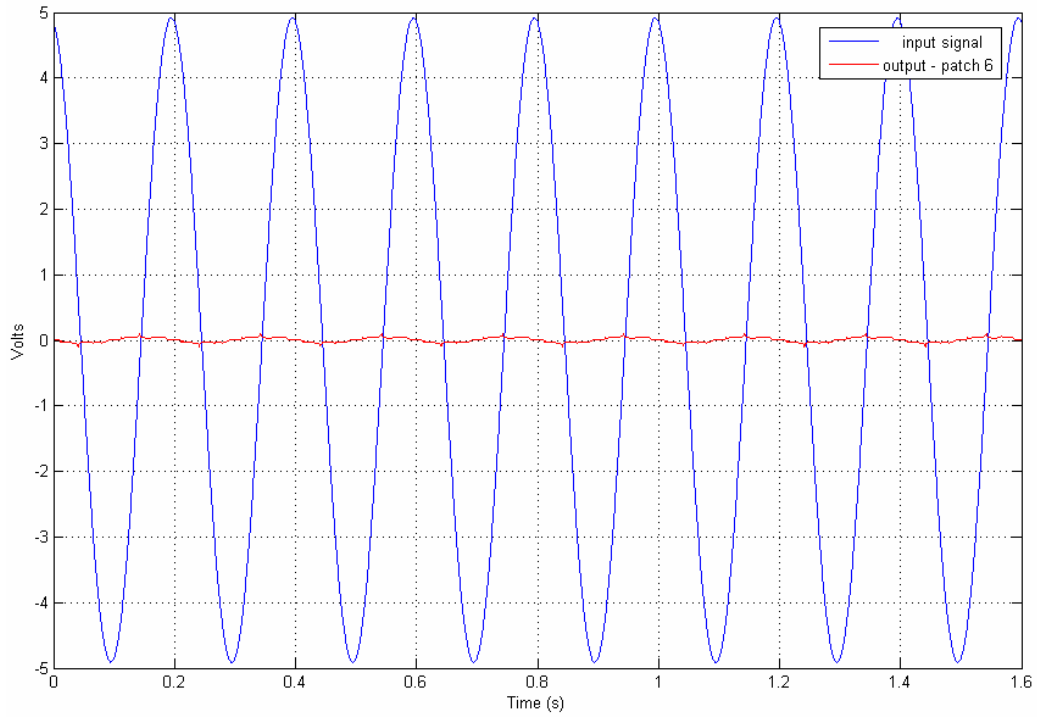


Figure 25: Time Response Showing Output to Five Hertz Sine Wave Input

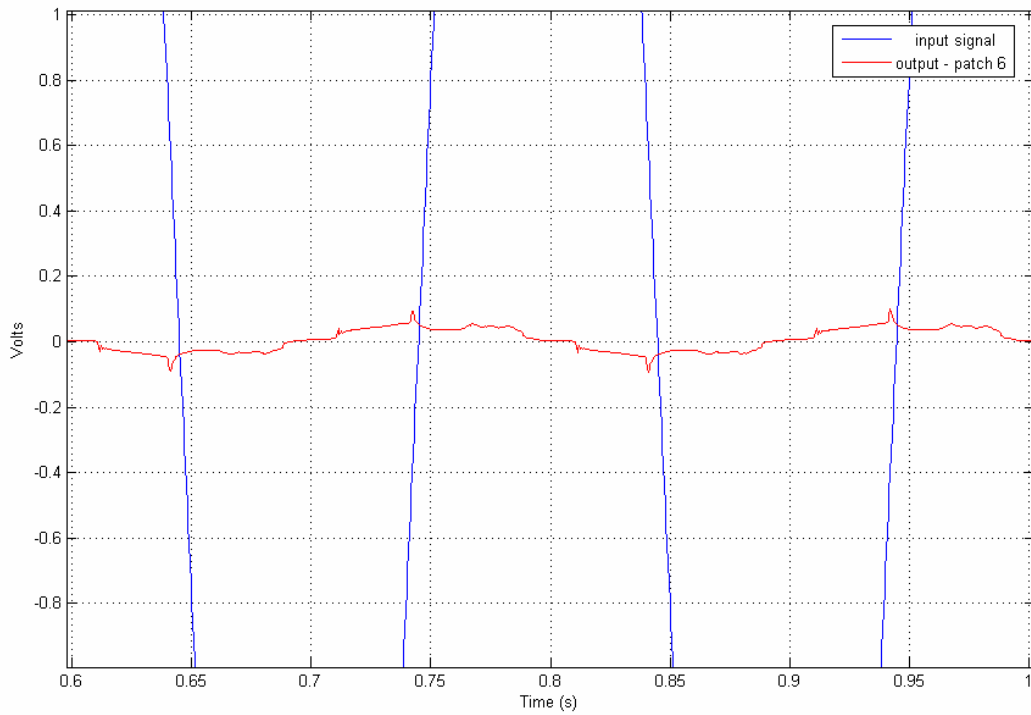


Figure 26: Time Response to Five Hertz Sine Wave (zoom view)

Figure 27 and Figure 28 show the same response to a 10-Hz sine wave.

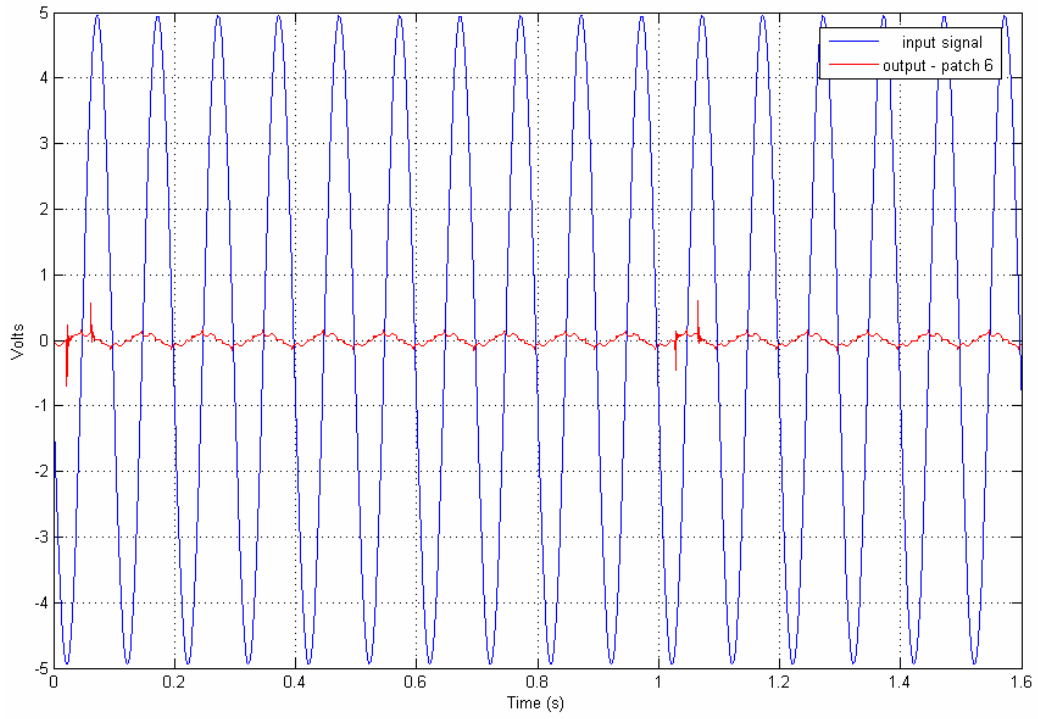


Figure 27: Time Response to 10 Hz Sine Wave

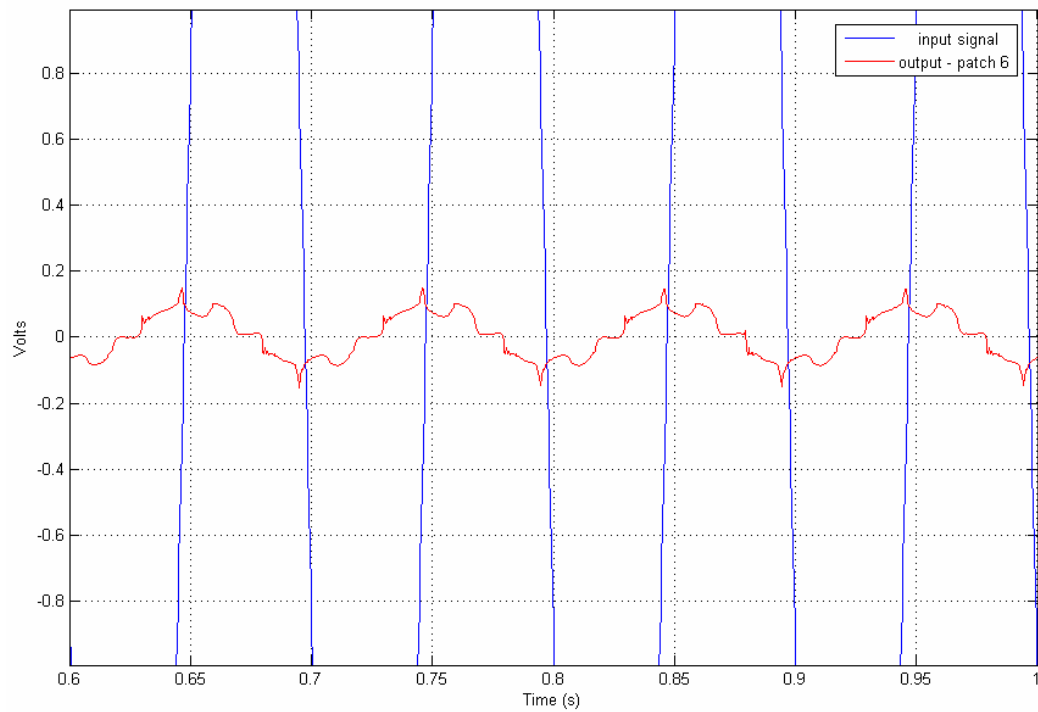


Figure 28: Time Response to 10 Hz Sine Wave (zoom view)

It can be seen from these graphs that the voltage on the patches does not approximate the input voltage well. This causes the response at the natural frequencies to be effectively damped due to the fact that the voltage response cannot resonate at that frequency since it cannot even approximate a sine wave at that frequency. As the frequency of the input signal increases, the output signal more closely resembles the input sine wave as can be seen from the following figures.

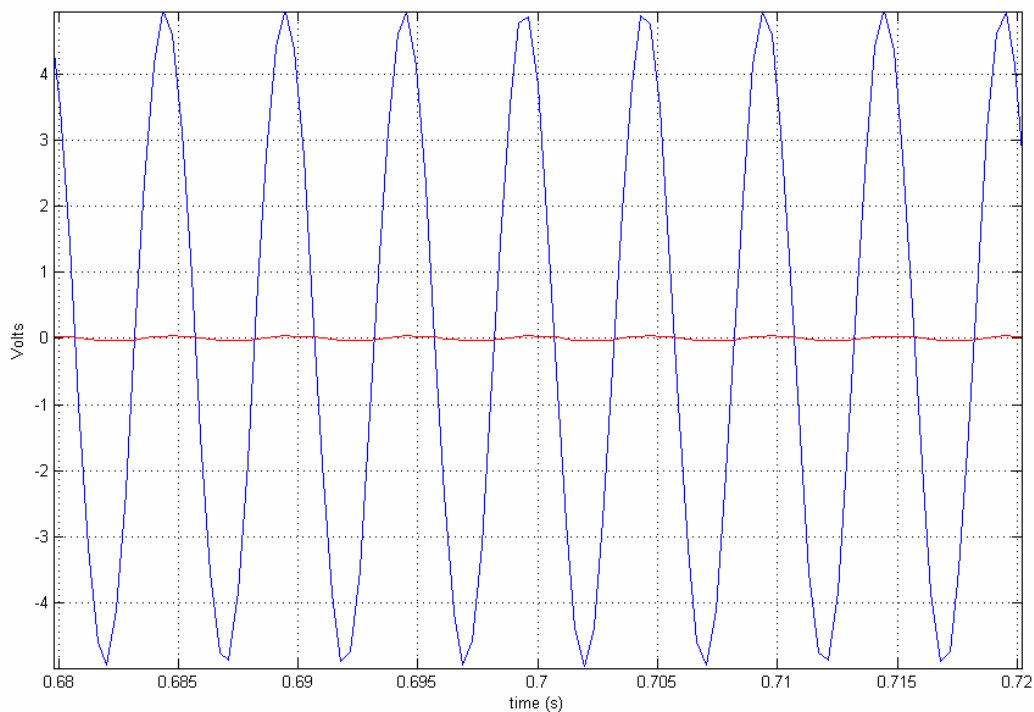


Figure 29: Time Response to a 200-Hz Sine Wave

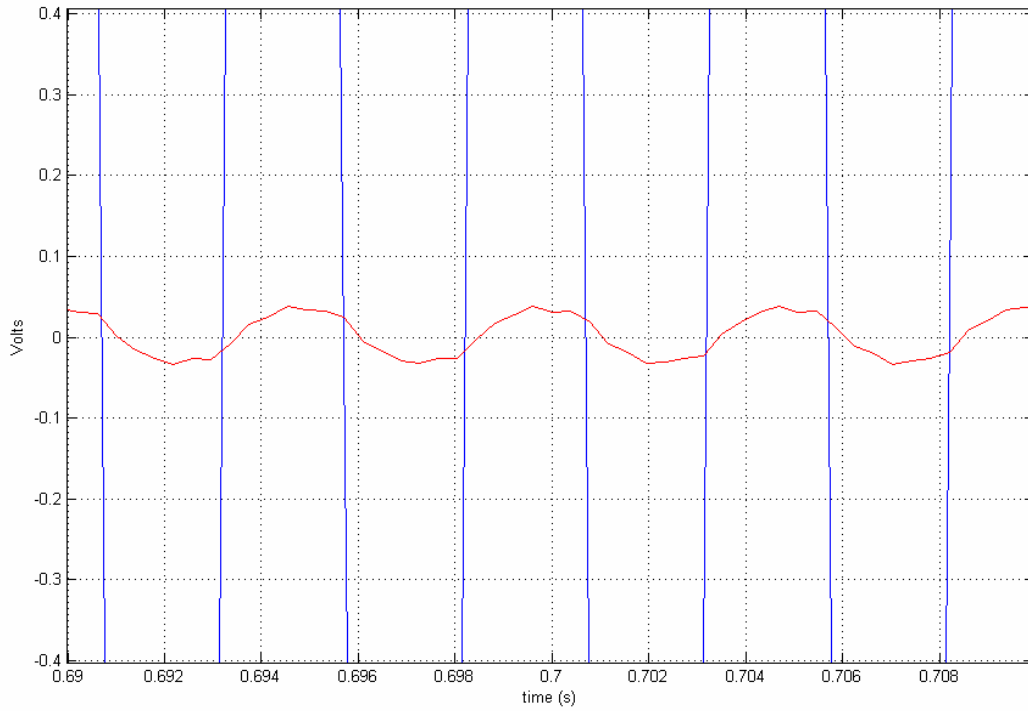


Figure 30: Time Response to 200-Hz Sine Wave (zoom view)

Because of this voltage dissipation phenomena, a new design of the circuit used to measure the voltage on the patches would have to be implemented in order to use the patches as sensors to detect surface deflection.

IV. Development of 61-Patch Mirror

4.1 Overview

With just seven sensors used to measure the surface deflection, the accuracy of the measured surface deflection does not correspond well to a Zernike decomposition. Jiang, Ling, Rao, and Shi give a formula to determine the minimum number of actuators required to distinguish a certain Zernike polynomial (8).

$$N_L = \frac{\pi}{4}(n - m + 2)^2 \quad (30)$$

N_L is the number of actuators required. The variables “m” and “n” describe the specific Zernike polynomial, where “m” designates the azimuthal frequency and “n” designates the radial degree.

Table 8 shows a pictorial representation of the Zernike polynomials.

Table 8: Pictorial Representation of Zernike Polynomials (13)

$n \setminus m$	0	1	2	3	4
0	piston 				
1		tilt 			
2	defocus 		astigmatism 		
3		coma 			
4	spherical 				

According to the formula given earlier, a 7-patch mirror will be capable of representing all of the terms in which “n” is equal to “m”. None of the other Zernike polynomials will be able to be represented accurately by using a 7-patch mirror. Because of this, a new design is needed if the patches are to be used for sensing and representing the surface. Part of the focus of this research was to develop a 61-patch actuator mirror. The value of 61 was selected in order to correspond to a mirror purchased from AgilOptics that can be used in later work for comparison.

4.2 Control Pattern Design

The control pattern is composed of a central patch with five concentric rings (see Figure 31).

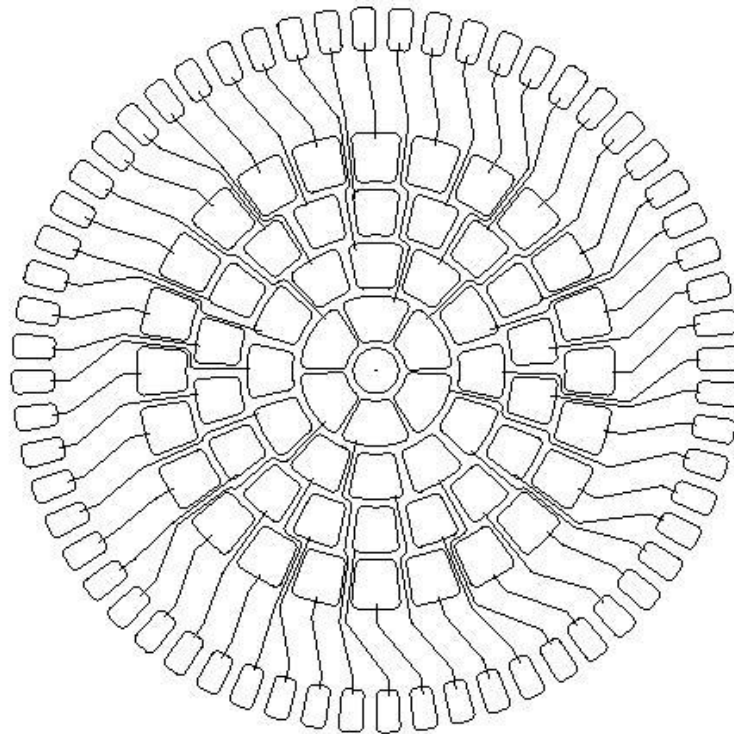


Figure 31: 61-Patch Mirror Design

The first four rings are the actual patches that will be used for sensing or actuating the surface. The outer ring is composed of the leads that will be connected to either the voltage input or to the data acquisition system. The center patch does not have a lead so a wire will have to be connected to it directly for it to be used. This was done to ease in the construction of the pattern mask that will be discussed later. The center patch has a radius of 0.0938 in. The first ring of patches consists of 6 patches each occupying a 55° extent with 5° spacing between them. The inner radius of this ring is 0.1321 in. and the outer radius is 0.3125 in. The second ring holds 12 patches with each one covering 25° with 5° spacing between each one. The inner radius is equal to 0.3437 in., and the outer radius is equal to 0.5312 in. The third ring has 18 total patches. Each of these has 5° spacing between patches while the patch itself takes up 15° . The inner radius of this ring is 0.5624 in., and the outer radius is 0.7499 in. The last of the rings that is used for actual manipulation of the surface is the fourth ring. It contains 24 patches each spaced 3° apart and covering 12° . The inner and outer radii of this ring are 0.7811 in. and 0.9843 in. respectively. The final ring is used to hold the leads. This ring contains 60 patches that cover 4° and are separated by 2° . The inner radius of this ring is 1.325 in., and the outer radius is 1.5 in.

The first step in transferring the pattern to a piece of PVDF material is to generate a mask that will allow light to pass through to the mirror wherever there is not a patch or a lead. This was done by a company called Bandwidth Foundry. The mask is a glass substrate with the pattern etched onto it so that light will not pass through in those areas. Figure 32 shows a picture of the mask that was used.



Figure 32: Mask Used For Transferring Pattern to PVDF

4.3 Fabrication Process

To start the fabrication process, a 4-in. diameter circle of PVDF material is cut out. The piece of PVDF material must have a maximum diameter of 4-in. because of limitations in the equipment available. The one-direction is marked with two small lines parallel to the one-direction on the right side and one small parallel line on the left side. These marks are made on the negative side of the PVDF. These marks will ensure that the mirror will later be able to be oriented in the same direction for each test. After the piece of PVDF is prepared, it is taken to the clean room to continue with the fabrication process. The first step is to coat a 4-in. silicon wafer with photo-resist. This is done by spinning and applying a small amount of photo-resist to the center of the wafer. The spinning action will cause the photo-resist to be spread evenly over

the entire wafer. Once the wafer is coated the PVDF material is placed on the wafer with the positive side facing up. The wafer with the PVDF material on it is then placed on a hot plate heated to 60° C. This will cause the photo-resist to harden, and it will act like a bond between the wafer and the PVDF. Once the PVDF is sufficiently bonded to the wafer the wafer is again put on the spinning apparatus and more photo-resist is applied to the positive side of the PVDF material. Again, this layer of photo-resist is spread evenly over the entire PVDF. The wafer is then placed on the hot plate again to cure the photo-resist. This is done for approximately 10 minutes. After this is done, the wafer is placed in the wafer mask aligner and the mask is placed on top of it so that the PVDF is between the wafer and the mask. The mask aligner has an aperture of 4-in. This is what creates the limitation on the size of the mirror. With different equipment, there is no limitation on the size of the mirror that can be manufactured. Figure 33 shows a picture of the mask aligner.

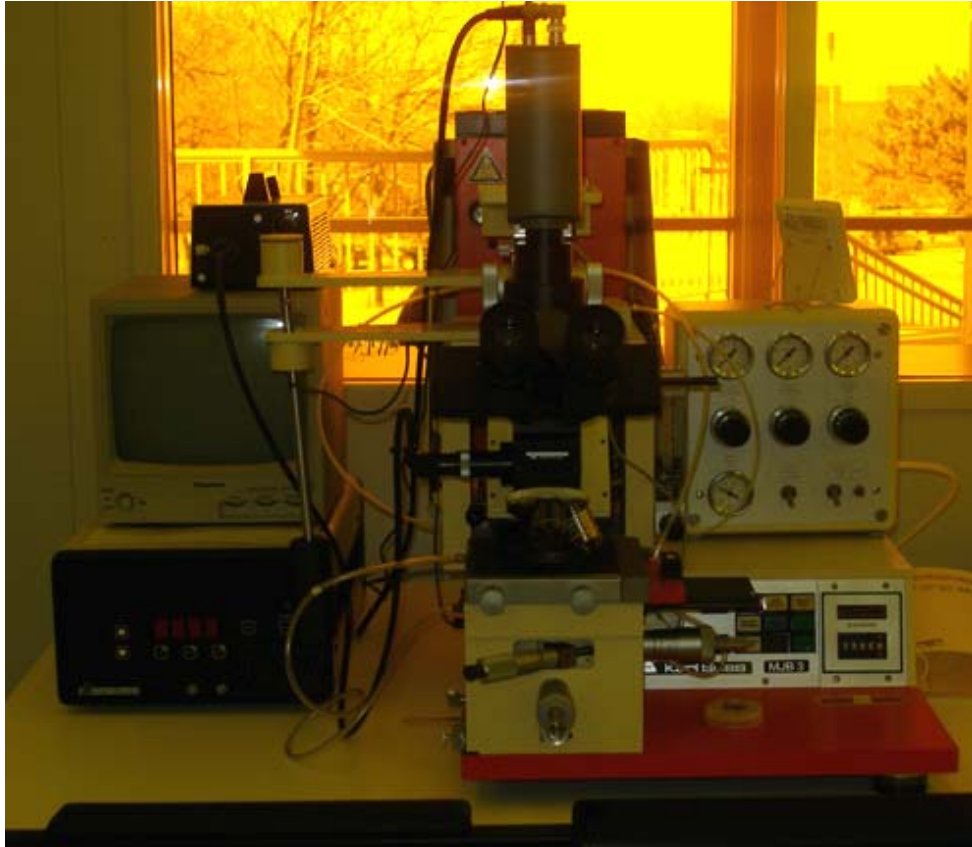


Figure 33: Wafer Mask Aligner

Great care must be taken in order to line up the mask with the aperture of the mask aligner. If it is not lined up so that ultra-violet light shines on the entire mask the process will have to be repeated. Once everything is lined up correctly the PVDF is exposed to UV light. This causes the photo-resist on the exposed areas to be subject to a developer while the areas that are not exposed will not be subject to the developer. After the exposure the wafer is taken out of the mask aligner and is washed in a developer bath. The developer removes the photo-resist from those areas that were exposed to the UV light. This will take 3-5 minutes.

When the sample is fully developed it can then be etched using the ferric chloride mentioned earlier. The entire positive surface is etched with the ferric chloride. This was done by coating the entire surface with ferric chloride and then washing it off with water in order to stop the reaction. The sample is then taken back to the clean room and is treated with acetone to

remove the photo-resist. The sample needs to be submersed in acetone in order to remove the PVDF from the plate. The negative side of the PVDF is then etched with the ferric chloride in order to provide for an even surface. The sample is now ready for tensioning and mounting.

4.4 Tensioning and Mounting

In order to tension such a small specimen, a new method needs to be devised. This is accomplished by cutting a 14 in. by 14 in. piece of PVDF material. A circle of diameter 4.25 in. is then cut out of the center of this piece of PVDF material. The etched piece of material is then taped into the center of this hole using masking tape, taking care to ensure that it is exactly centered. The large piece of PVDF is placed in the tensioning apparatus as described previously and the tensioning is done the same way as one layer of the two-layer mirror was done.

The next step is to epoxy the mounting ring to the surface. The mounting ring had to be redesigned in order to accommodate the reduced size of the mirror. This was done by taking the original design and scaling it so that it would fit the new mirror. Figure 34 shows the new design of the aluminum ring.

Material: 7075T6 Aluminum

All dimensions in inches

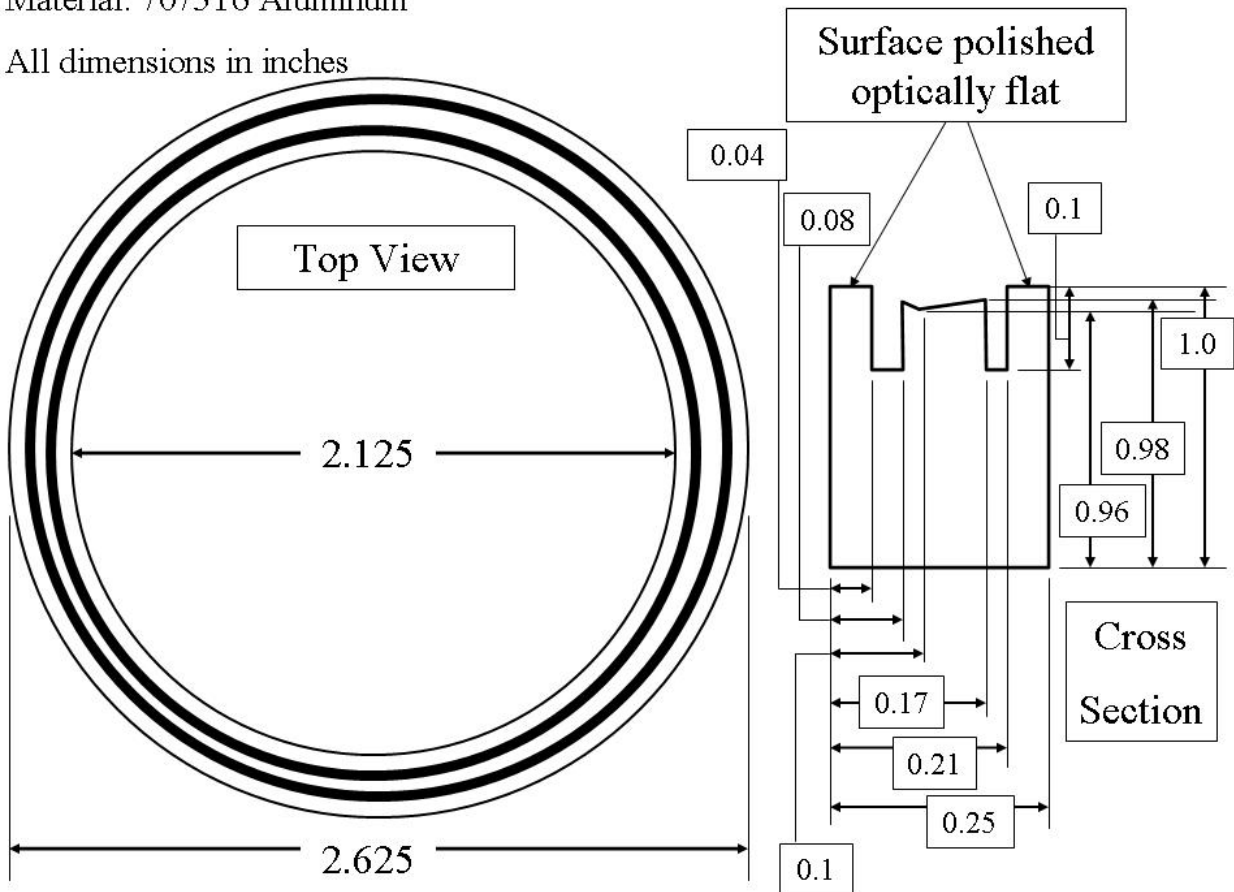


Figure 34: Aluminum Ring Design for 3-in. Mirror

The ring was epoxied to the surface of the PVDF in the same manner as previously described for the larger ring. The only difference was that the epoxy in the grooves did not take as long to set. So the ring was placed on the PVDF only 20 minutes after the epoxy was put into the grooves. The final step in the manufacturing process is to coat the mirror with silicon and a thin layer of gold. This is done exactly as is outlined by Trad (17). Figure 35 shows the final mirror before silicon coating is applied.

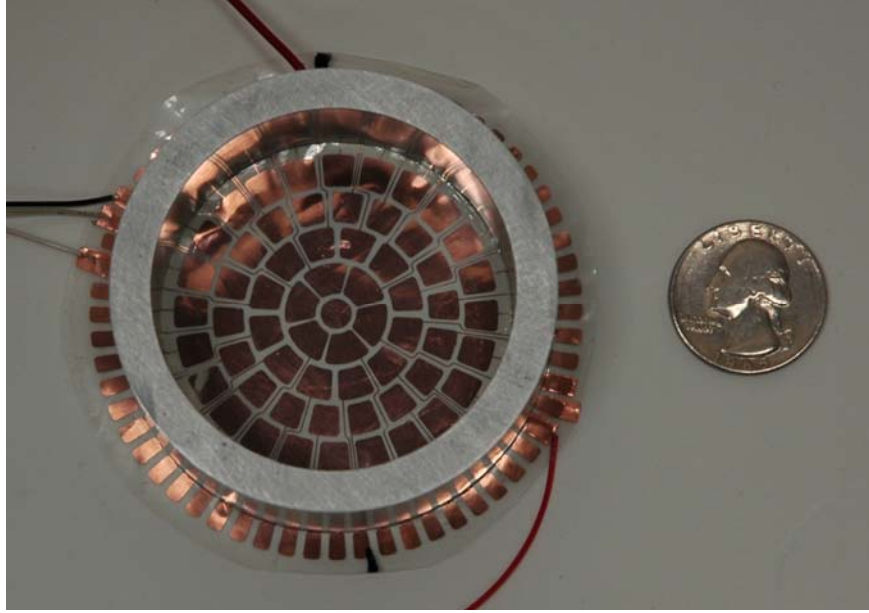


Figure 35: 61-Patch Mirror Without Silicon Coating

V. Testing of 61-Patch Mirror

5.1 Overview

The testing on the 61-patch mirror was done similar to the two-layer mirror described earlier. The difference is that the only input used was an acoustic source. This was because the objective was mainly to validate the fabrication process mentioned previously as opposed to showing the deformation caused by actuation through the patches. A test using the SignalCalc data acquisition system was performed as well as a test using the laser vibrometer as the data acquisition system. The results of these two tests were compared.

5.2 Patch Measurement Test

The input source which was chosen for this test was a speaker manufactured by HiVi research. The model that was used was the F6 model. Table 9 shows the operational parameters of this speaker.

Table 9: Operational Parameters for Acoustic Source (16)

Nominal Impedance (Z)(Ω) :	8
Resonance Frequency (Fs)(Hz) :	45
Nominal Power Handling (Pnom)(W) :	45
Max Power Handling (Pmax)(W) :	90
Sensitivity (2.83v/1m)(dB) :	88
Weight (M)(Kg) :	2.1
VC Diameter (mm) :	25
DC (Re)(Ω) :	6.5
VC Length (H)(mm) :	14.5
VC Former :	SV
VC Frame :	Kapton
Magnet System :	Shielded
Magnet Former :	Ferrite
Force Factor (BL)(TM) :	9.0
Gap Height (He)(mm) :	6.0
Linear Excursion (Xmax)(mm) :	4.3
Suspension Compliance (Cms)(uM/N) :	658
Mechanical Q (Qms) :	3.91
Electrical Q (Qes) :	0.38
Total Q (Qts) :	0.35
Moving Mass (Mms)(g) :	18.3
Effective Piston Area (Sd)(m ²) :	0.0139
Equivalent Air Volume (Vas)(L) :	16.4
Cabinet Type :	Vented
Recommended Box Volume(Vb)(L) :	15
Tuning Frequency(Fb)(Hz) :	45
-3dB Cut-Off Frequency(F3)(Hz) :	42

The data acquisition system used for this first test was the SignalCalc computer described earlier.

There were not enough leads to measure all of the patches at once. Therefore, three different tests were run, measuring 8 patches each time. Figure 36 shows which patches were measured as well as the numbering scheme used to refer to the patches. Patches 2, 8, 20, 38, 5, 14, 29, and 50 correspond to the one-direction of the material.

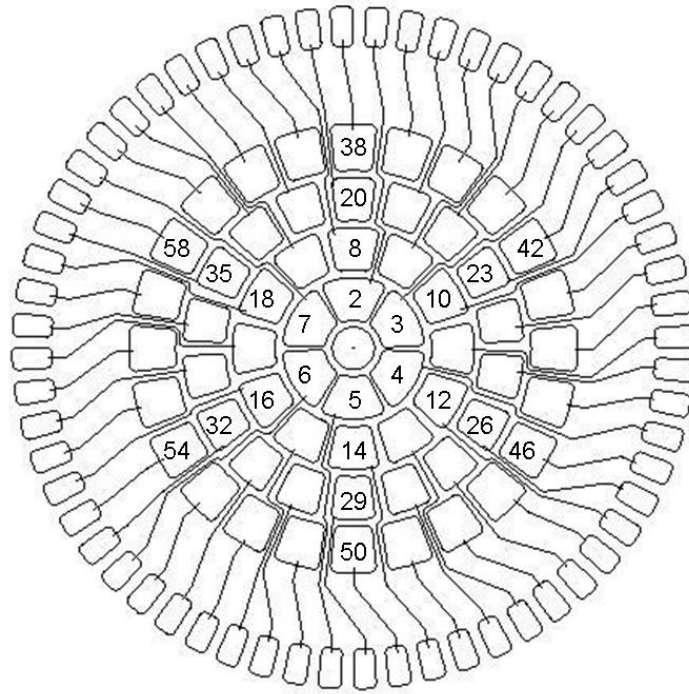


Figure 36: Patches Measured During Test

The first test was done measuring one radial direction corresponding to the one-direction and measuring one radial direction not parallel with the one-direction. One thing that was noticed during the test was that the FRF's measured off the patches aligned with the one-direction were much clearer than the response from the other patches. Figure 37-Figure 40 show the results broken up by concentric ring. The difference in measured FRF was clear for rings 1-3 but not as clear for the fourth ring. This could have been because the data in general was poor for the fourth ring because it was right up against the edge of the mirror.

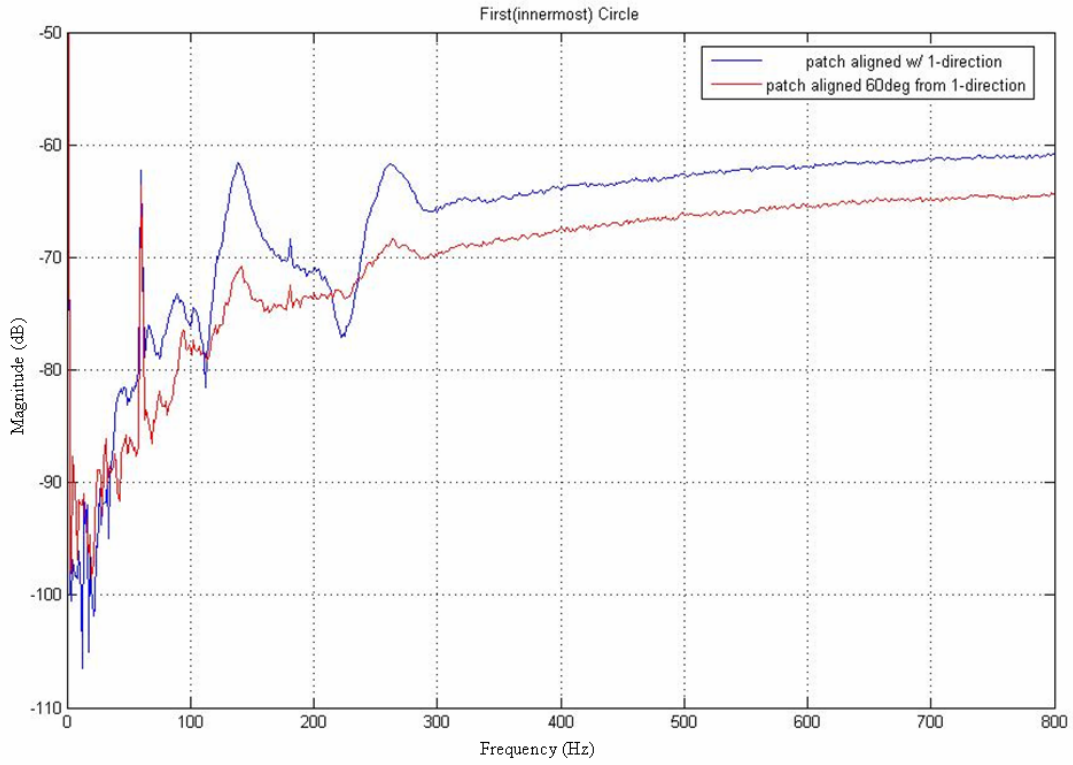


Figure 37: Comparison of One-Direction with Another Direction - First Ring

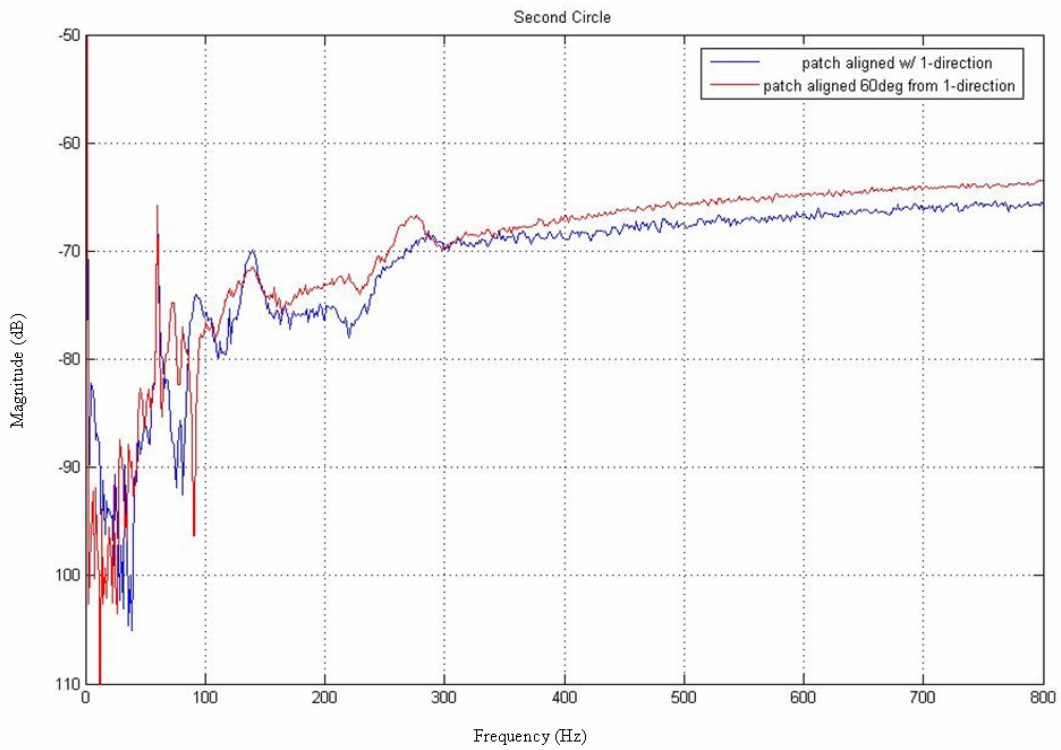


Figure 38: Comparison of One-Direction with Another Direction - Second Circle

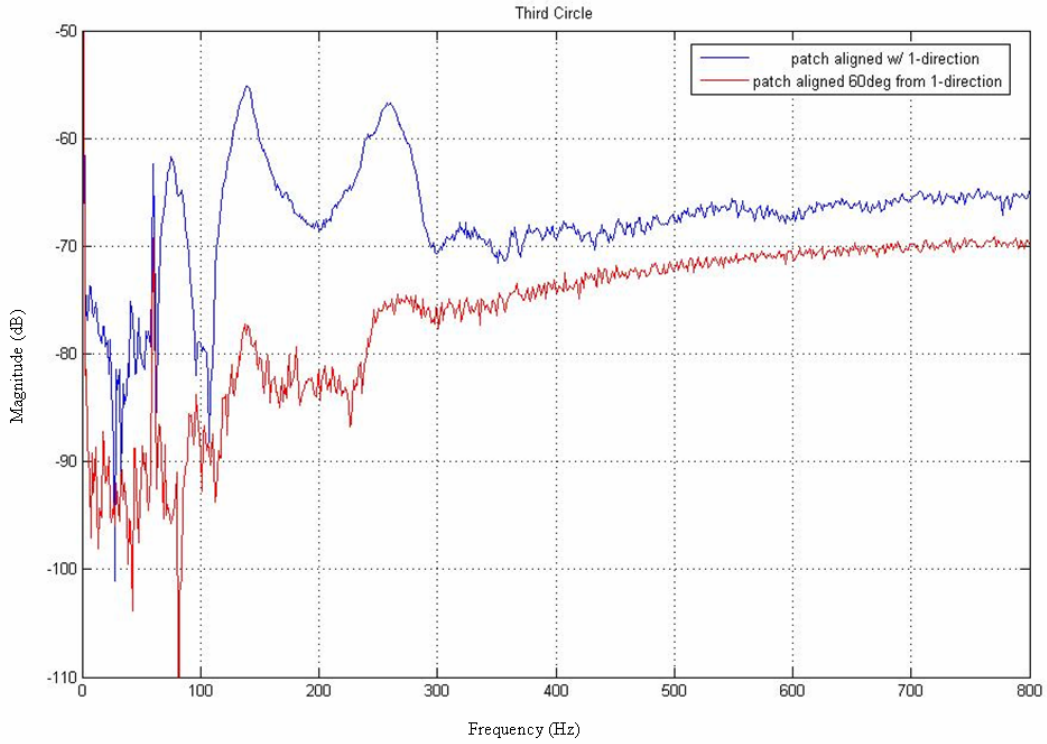


Figure 39: Comparison of One-Direction with Another Direction - Third Circle

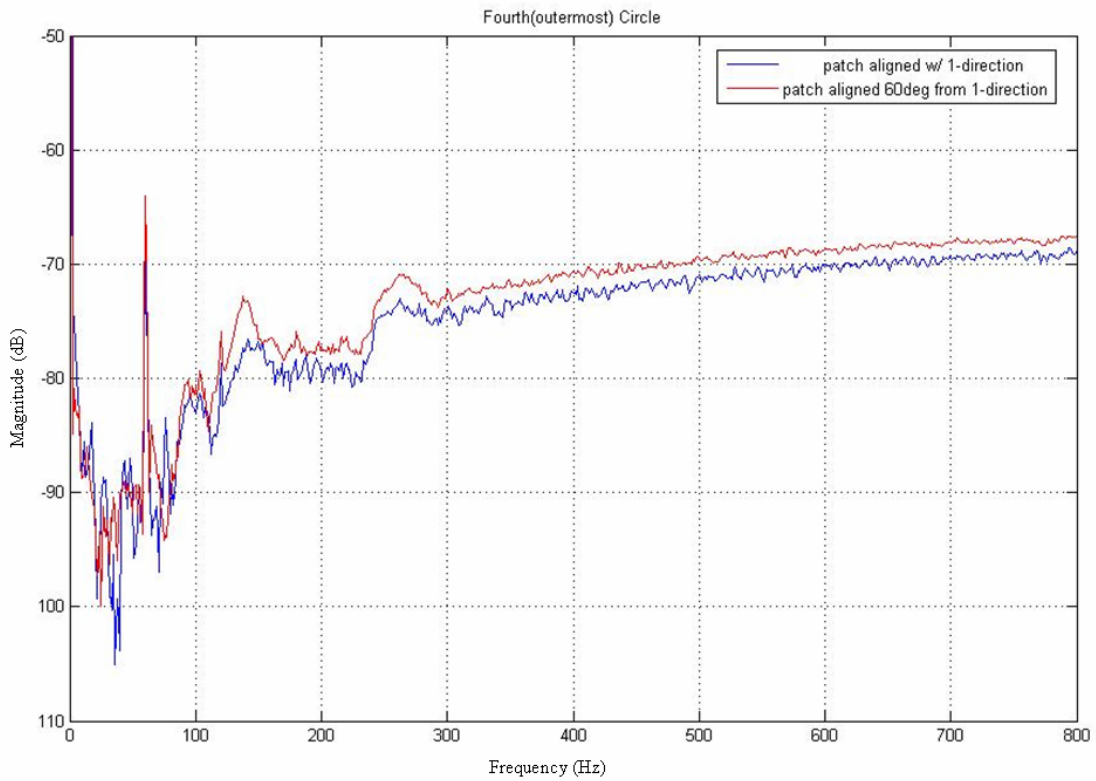


Figure 40: Comparison of One-Direction with Another Direction - Fourth Circle

The first two vibrational modes were determined from the FRF's that were calculated. These modes were found at 140 Hz and 260 Hz. One difficulty that was encountered was that each test registered a large spike at 60 Hz and subsequent smaller spikes at multiples of 60 Hz. These were obviously caused by the lighting in the room operating at 60 Hz and were discounted. They often corrupted the data and multiple tests had to be run in order to get good data. The following figures show the FRF's for two radial directions parallel to the one-direction and for another of the radial directions. Please see Appendix B for all of the results from this test.

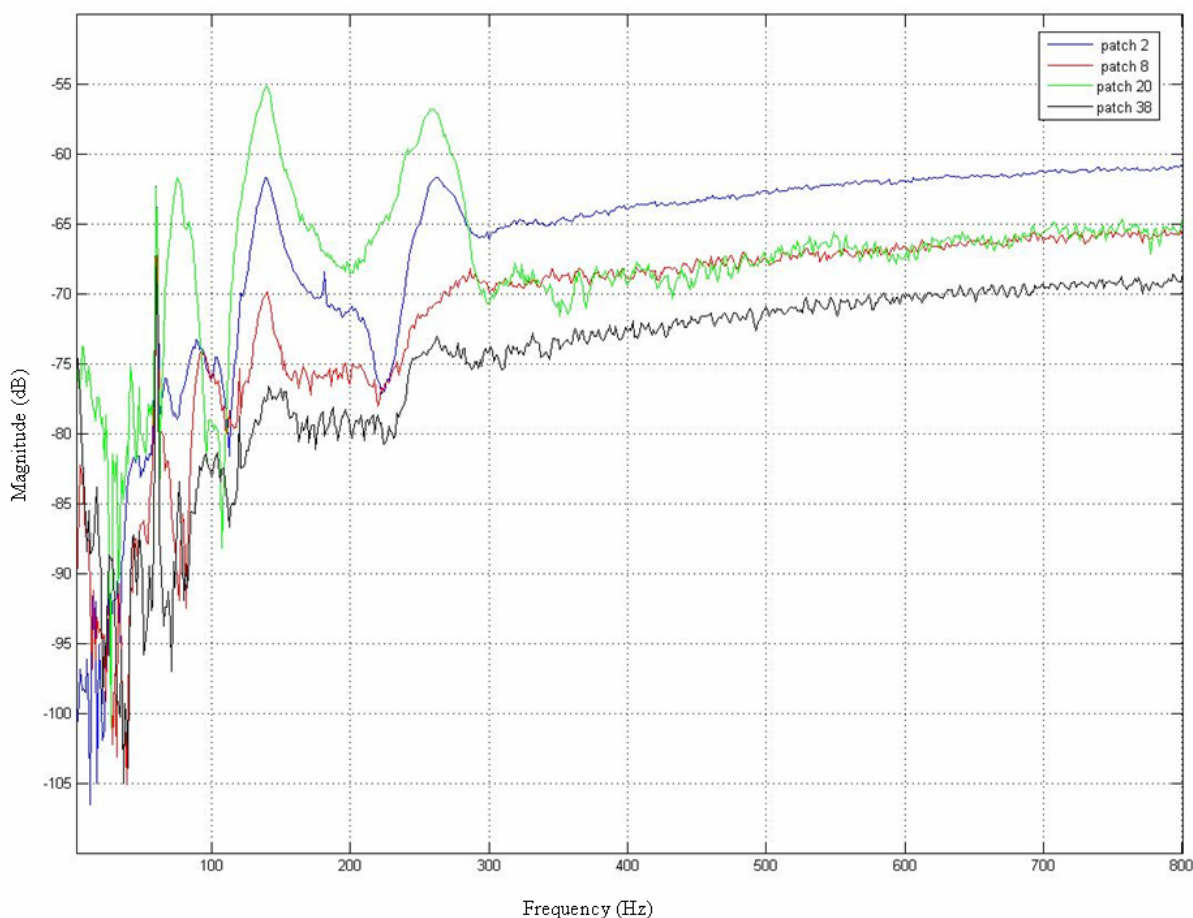


Figure 41: FRF's for Patches 2, 8, 20, and 38

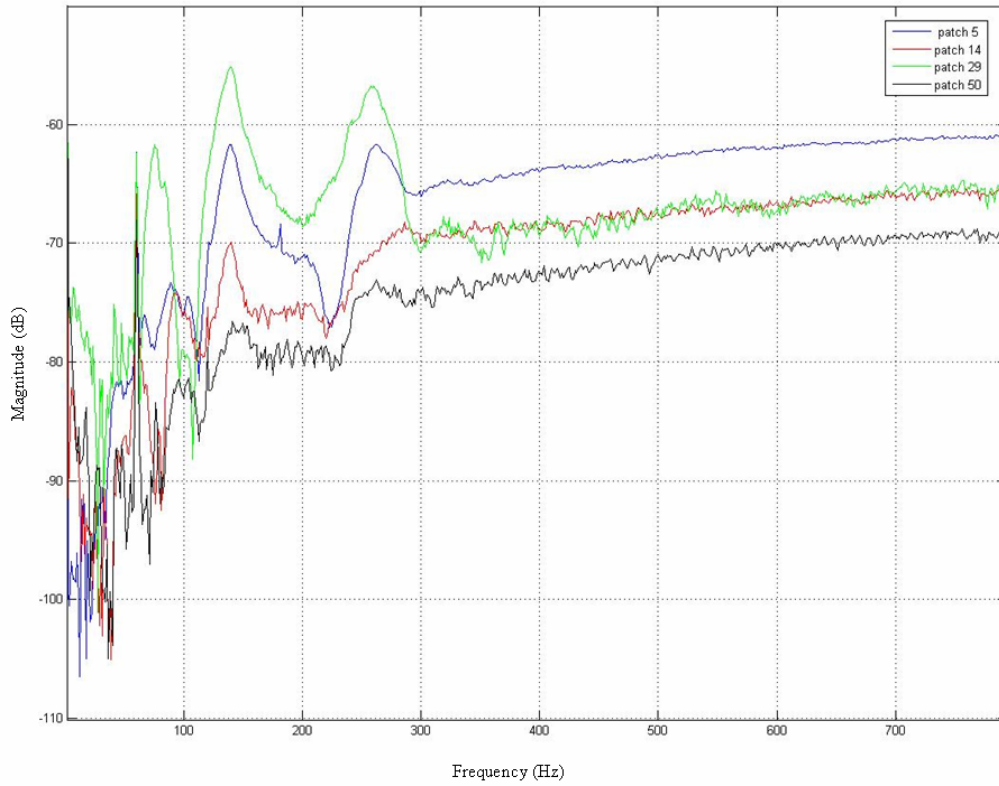


Figure 42: FRF's for Patches 5, 14, 29, and 50

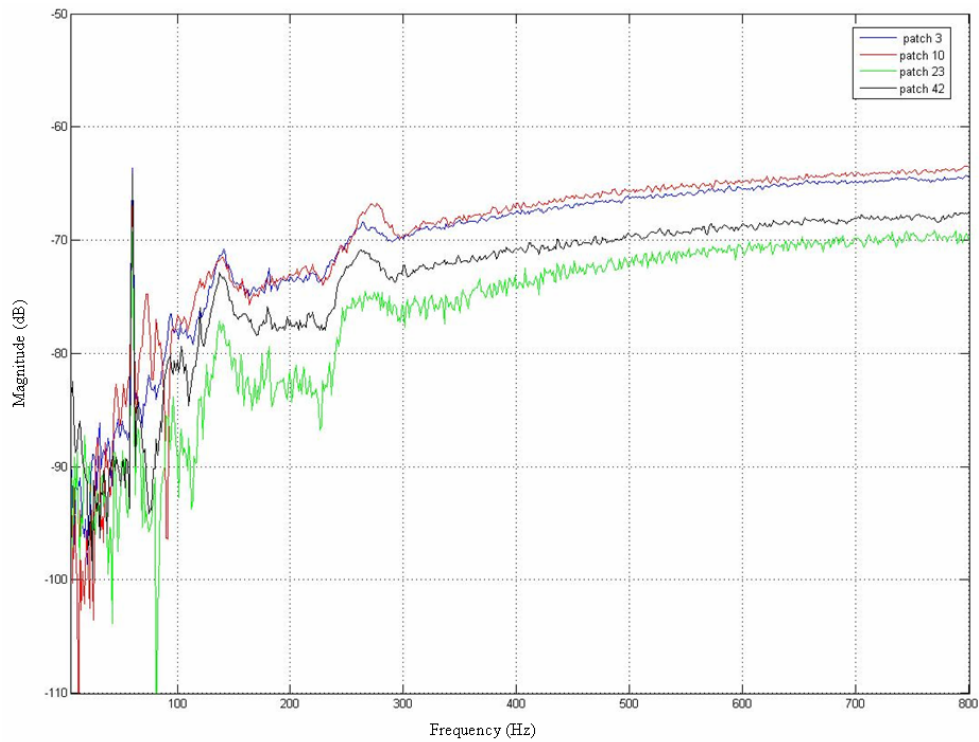


Figure 43: FRF's for Patches 3, 10, 23, and 42

It is apparent from these plots that there is a similar voltage dissipation issue with this mirror as well. The magnitude of the values over 300 Hz are very similar to the values shown from the 7-patch mirror earlier.

5.3 Laser Vibrometer Test

The second test performed on the 61-patch mirror was to use the same acoustic input device but measure the FRF using a scanning laser vibrometer. The test was set up in the same way that the laser vibrometer test conducted by Trad (17) was set up (see Figure 44 and Figure 45).



Figure 44: Laser Vibrometer Test Setup

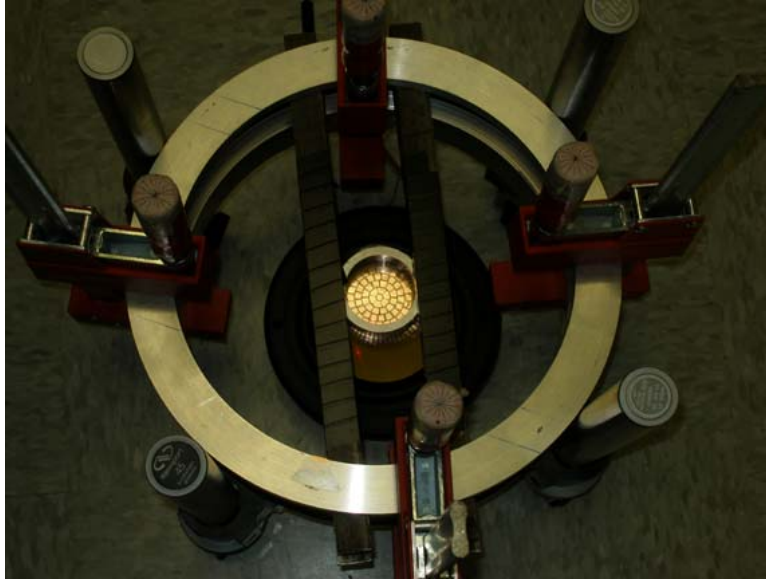


Figure 45: Close-Up of Mirror in Laser Vibrometer Test Setup

The test results showed different values for the first two modes. This is because during the laser vibrometer test the mirror was clamped down using the tensioning apparatus while it was sitting free with nothing holding it down during the patch response test. This clamping could be enough to move the first mode from 140 Hz to 170 Hz and to move the second mode from 260 Hz to 302 Hz. Figure 46 shows the comparison of the two FRF's.

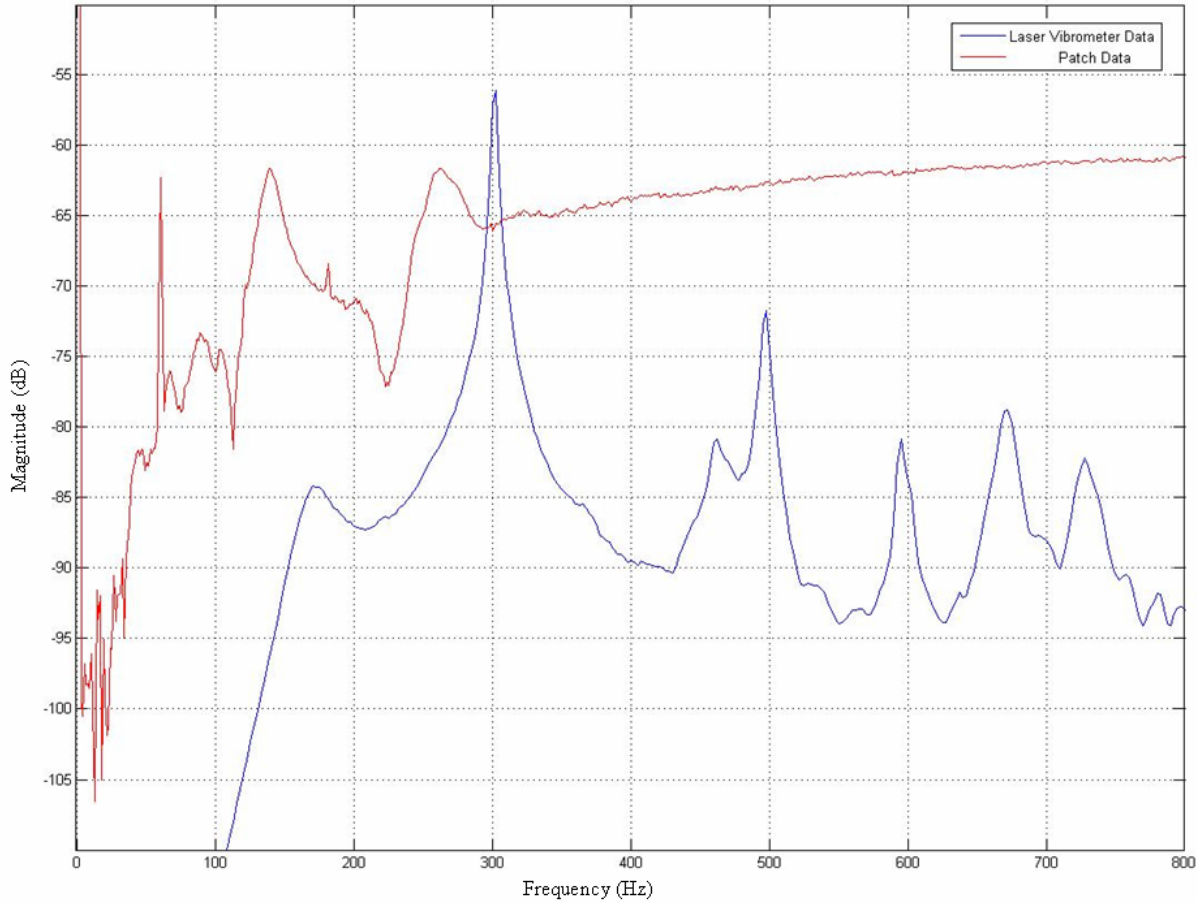


Figure 46: Comparison of FRF's From Two Tests

Another difference between the two tests that was not accounted for was the fact that the laser vibrometer test measured the movement of the entire surface as a whole while the patch tests measure the movement of each of the patches individually. One area for future study would be to set up a grid using the laser vibrometer that only measures one patch at a time and compare the results to the results from the patch test. The conclusions drawn from this test will be discussed in the next chapter.

VI. Conclusion and Recommendations

6.1 Overview of Experiment

This research contained the development of a method to sense the surface deflection of a deformable mirror using the PVDF material as a sensing mechanism. An overview of the experiments on a two-layer mirror as well as the experiments on a 61-patch mirror is provided.

6.1.1 Sensing Method

A new sensing method to determine the surface deflection was developed. This consisted of fabricating a two-layer mirror and using the top layer to measure voltages from the patches on the mirror. The second layer was used as a means of actuation. An outline of a control scheme involving a state-space representation of the mirror as well as a method of converting voltages to Zernike coefficients is presented. The mirror was subjected to tests using a scanning laser vibrometer to measure displacement as well as using the PVDF material as a method for measuring voltage. Results from these tests are also presented.

6.1.2 Development of 61-Patch Mirror

Because more actuators/sensors are required in order to sufficiently achieve desired Zernike shapes, a new design had to be developed. The methods used to manufacture a 61-patch, 2-in. diameter mirror are discussed. This includes the design of the control pattern as well as the fabrication steps.

6.1.3 Testing of 61-Patch Mirror

The results of two different tests conducted on the 61-patch mirror are presented. The first of these is a test measuring the voltage coming from various patches under the influence of an acoustic source. The second of these is a test measuring the surface deflection using a scanning laser vibrometer. A comparison between these two tests is presented and possible reasons for differences are given.

6.2 Conclusions Drawn

6.2.1 Sensing Method

The plate equation showed slightly better results when compared with the measured values than the membrane equation. The predicted modes were closer but there was no noticeable difference in the mode shapes themselves. The actual equation governing the dynamics of the deformable mirror is a combination of these two equations.

The method developed for measuring voltages off the patches in order to develop a state-space model did not give the anticipated results. This was determined to be because of the dissipation of the voltage from the patches. This caused the response from the patches to not be able to track a sine wave at low frequencies. More testing needs to be done to characterize this effect.

6.2.2 Development of 61-Patch Mirror

This process contributed the most value to the development of deformable mirrors. Before this method was developed, researchers at AFIT had only been able to manufacture a

seven patch mirror due to a practical limit introduced by hand-etched patterns. The method developed through this research worked extremely well in transferring a higher density control pattern to the PVDF material. Great care was taken to ensure that the process used was repeatable. It was determined that a better method of ensuring the alignment of the wafer with the ultraviolet light aperture is required. This is the only part of this fabrication process that requires further improvement.

6.2.3 Testing of 61-Patch Mirror

The testing process for the 61-patch mirror proved to be more difficult than the testing of the two-layer mirror. The two tests conducted did not properly line up for a number of different reasons. Overall, this test showed that the fabrication method discussed previously was valid. The voltage dissipation issue was evident here as well so measuring the voltages as a way to determine surface deflection would not be valid for this mirror either without a new design of the measurement method. Therefore, more work needs to be done in this area to properly characterize these sensors.

6.3 Areas for Further Development

This research opened up many possible areas for future study. It is the author's desire that these topics will be explored further in the future.

6.3.1 Sensing Method

This area provided the most room for improvement. The equations governing the displacement of the mirror need to be determined so that they match with experimental values. Once this is done, a control scheme such as dynamic inversion can be easily implemented.

The measuring of the FRF's from the patches also requires a lot of work. First of all, a method for negating the effects of the voltage dissipation needs to be implemented. Additionally new designs for the patch configuration could be tried so that there is more cross-talk between patches. Perhaps a four-layer design such as that proposed by Lee, Elliot, and Gardonio needs to be considered (9). There are other designs that could be tried such as not aligning the two layers exactly but offsetting them by some angle. These designs all need to be explored in order for a valid state-space model to be calculated from the patches.

6.3.2 61-Patch Mirror

There are a number of areas that are available for future research in developing smaller actuator patterns. The first of these is possible changing the actuator shape and placement. It was noted during the course of testing that those patches that were aligned with the one-direction of the material produced clearer output than the other patches. Perhaps a pattern that utilizes rectangular patches all aligned with the one-direction of the material would be more useful than the pattern developed through this research.

The second area for future research is better characterization of the patches as sensors. The largest area for further research in this area is also a better characterization of the dissipation of voltage from the patches. This is true for any sensing using the PVDF material and is the most important take-away from this research.

6.4 Summary

This project consists of the development of a sensing method for sensing surface displacement of deformable mirrors, the design of a 61-patch mirror and the testing of the same 61-patch mirror. All relevant details concerning these three areas have been presented and discussed. This research has made significant advances in the area of manufacturing deformable membrane mirrors.

This development has brought within reach closed loop control of a deformable mirror. This is a critical step in the development of large aperture space telescopes, which are the future of the US space surveillance program.

Appendix A: Matlab Code for Generating Mode Shapes

A.1 Plate Equation Mode Shapes

```
r_max=1; % radius of mirror in inches
h_r=0.005; % distance between circumferential grid points in inches
h_theta=pi/(4*36); % distance between radial grid points in radians
r_vector=0:h_r:r_max;
theta_vector=0:h_theta:350*pi/180;
r_vector=r_vector';
theta_matI= repmat(theta_vector, size(r_vector,1),1);
r_matI= repmat(r_vector,1, size(theta_vector,2));
p=size(r_vector,1);
m=size(theta_vector,2);
%
BETA=[3.196 6.306 9.439 12.58;4.611 7.799 10.96 14.11;5.906 9.197 12.4
15.58;7.144 10.54 13.79 17.01];
n=0;
beta=BETA(n+1,1);
wc_nm=(besseli(n,beta)*besselj(n,beta*r_mat)-
besselj(n,beta)*besseli(n,beta*r_mat)).*cos(n*theta_mat);
ws_nm=(besseli(n,beta)*besselj(n,beta*r_mat)-
besselj(n,beta)*besseli(n,beta*r_mat)).*sin(n*theta_mat);
%
x=-r_max:h_r:r_max;
y=-r_max:h_r:r_max;
for j=1:size(y,2)
    for i=1:size(x,2)
        r=(x(i)^2+y(j)^2)^0.5;
        theta=atan2(y(j),x(i));
        if theta<0
            theta=theta+2*pi;
        end
        if r>r_max
            wc_nm_cart(i,j)=0;
            ws_nm_cart(i,j)=0;
        elseif round((r/r_max)*p)==0 & round((theta/(2*pi))*m)==0
            wc_nm_cart(i,j)=wc_nm(1,1);
            ws_nm_cart(i,j)=ws_nm(1,1);
        elseif round((theta/(2*pi))*m)==0;
            wc_nm_cart(i,j)=wc_nm(round((r/r_max)*p),1);
            ws_nm_cart(i,j)=ws_nm(round((r/r_max)*p),1);
        elseif round((r/r_max)*p)==0
            wc_nm_cart(i,j)=wc_nm(1,round((theta/(2*pi))*m));
            ws_nm_cart(i,j)=ws_nm(1,round((theta/(2*pi))*m));
        else
            wc_nm_cart(i,j)=wc_nm(round((r/r_max)*p),round((theta/(2*pi))*m));
            ws_nm_cart(i,j)=ws_nm(round((r/r_max)*p),round((theta/(2*pi))*m));
        end
    end
end
end
```

A.2 Membrane Equation Mode Shapes

```

r_max=1; % radius of mirror in inches
h_r=0.005; % distance between circumferential grid points in inches
h_theta=pi/(4*36); % distance between radial grid points in radians
r_vector=0:h_r:r_max;
theta_vector=0:h_theta:2*pi;
r_vector=r_vector';
theta_mat= repmat(theta_vector, size(r_vector,1),1);
r_mat= repmat(r_vector, 1, size(theta_vector,2));
p=size(r_vector,1);
m=size(theta_vector,2);
%
BETA=[2.4048 5.5201 8.654 11.791;3.8317 7.0153 10.173 13.324;5.1355 8.417
11.62 14.796;6.3799 9.761 13.015 16.224];
n=3;
beta=BETA(n+1,4);
wc_nm=(besselj(n,beta*r_mat)).*cos(n*theta_mat);
ws_nm=(besselj(n,beta*r_mat)).*sin(n*theta_mat);
%
x=-r_max:h_r:r_max;
y=-r_max:h_r:r_max;
for j=1:size(y,2)
    for i=1:size(x,2)
        r=(x(i)^2+y(j)^2)^0.5;
        theta=atan2(y(j),x(i));
        if theta<0
            theta=theta+2*pi;
        end
        if r>r_max
            wc_nm_cart(i,j)=0;
            ws_nm_cart(i,j)=0;
        elseif round((r/r_max)*p)==0 & round((theta/(2*pi))*m)==0
            wc_nm_cart(i,j)=wc_nm(1,1);
            ws_nm_cart(i,j)=ws_nm(1,1);
        elseif round((theta/(2*pi))*m)==0;
            wc_nm_cart(i,j)=wc_nm(round((r/r_max)*p),1);
            ws_nm_cart(i,j)=ws_nm(round((r/r_max)*p),1);
        elseif round((r/r_max)*p)==0
            wc_nm_cart(i,j)=wc_nm(1,round((theta/(2*pi))*m));
            ws_nm_cart(i,j)=ws_nm(1,round((theta/(2*pi))*m));
        else
            wc_nm_cart(i,j)=wc_nm(round((r/r_max)*p),round((theta/(2*pi))*m));
            ws_nm_cart(i,j)=ws_nm(round((r/r_max)*p),round((theta/(2*pi))*m));
        end
    end
end
end

```

Appendix B: Additional Plots

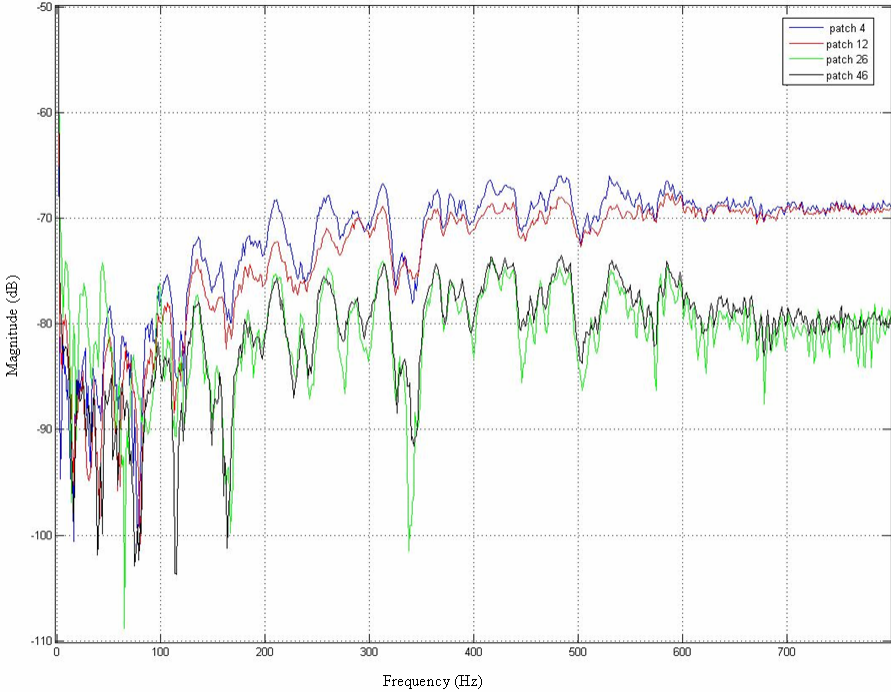


Figure 47: FRF's for Patches 4, 12, 26, and 46

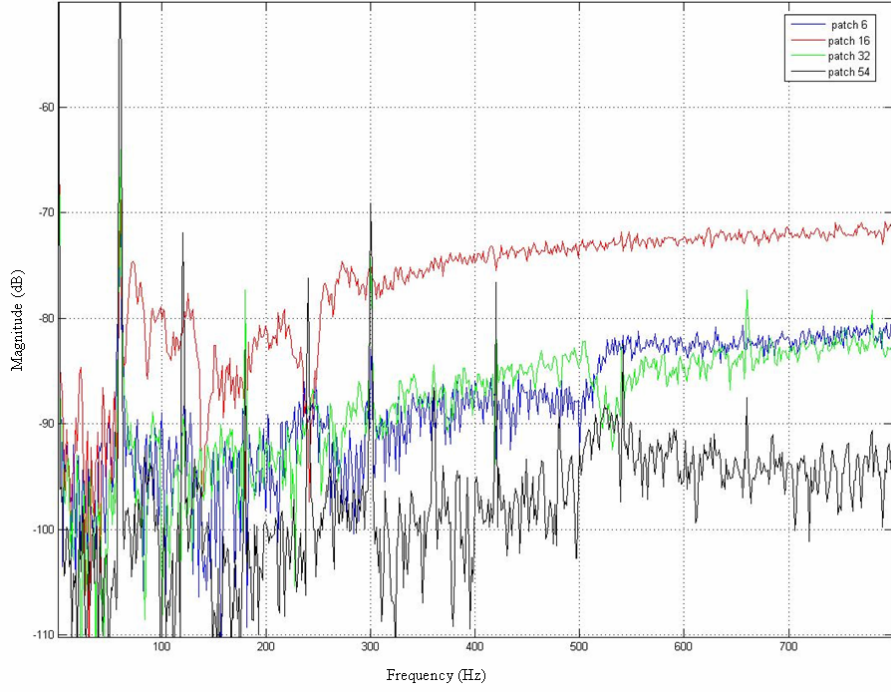


Figure 48: FRF's for Patches 6, 16, 32, and 54

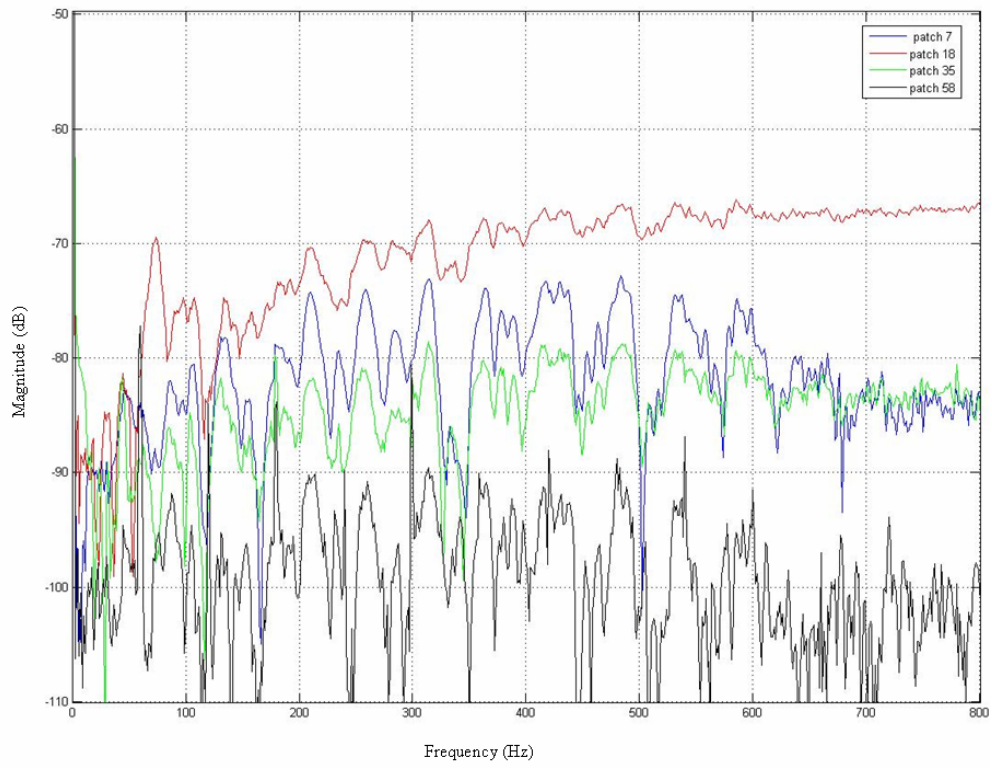


Figure 49: FRF's for Patches 7, 18, 35, and 58

Bibliography

1. Booth, Martin, Tony Wilson, Hong-Bo Sun, Taisuke Ota, and Satoshi Kawata. "Methods for the Characterization of Deformable Membrane Mirrors," *Applied Optics*, Vol. 44(24):5131-5139.
2. Cobb, Richard G. Lecture Notes, MECH 719, Oct-Dec 2005.
3. Ellis, Edric Mark. *Low-Cost Bimorph Mirrors in Adaptive Optics*. Diss. Imperial College of Science, Technology and Medicine, University of London, 1999.
4. Glanc, M, E. Gendron, F. Lacombe, D. Lafaille, J-F. Le Gargasson, P. Lena. "Towards Wide-Field Retinal Imaging With Adaptive Optics," *Optics Communications*, 230:225-238.
5. Hall, J., R. Glaese, and E. Flint. "Dynamic Behavior of Thin Film Membrane Strips," Proc. of AIAA/ASME/ASCE/AHS/ASC Structures, Structural Dynamics, and Materials Conference, 22-25 April 2002, Denver, Colorado.
6. Hammer, Jay A., Michele R. Banish, Michael R. Whitley, Zhili Hao, Keith O. Warren, Sharon Sanchez, John Harchanko. "Design and Fabrication of a Continuous Membrane Deformable Mirror," *SPIE Vol 4983 MOEMS and Miniaturized Systems III* (2003).
7. Hubblesite, "Hubblesite Website." Online at http://imgsrc.hubblesite.org/hu/db/1994/01/images/a/formats/large_web.jpg, January 2006.
8. Jiang, Wenhan, Ning Ling, Xuejun Rao, Fan Shi. "Fitting Capability of Deformable Mirror," *SPIE Vol. 1542 Active and Adaptive Optical Systems* (1991).
9. Lee, Young-Sup, Stephen J. Elliott, and Paolo Gardonio. "Distributed Four-Layer PVDF Actuator/Sensor Arrangement for the Control of Beam Motion," *SPIE Vol 4326 Smart Structures and Materials* (2001).
10. Main, John A., Jeffrey Martin, George Nelson. "Noncontact Shape Control of Membrane Mirrors," Proc. of Ultra Lightweight Space Optics Challenge Workshop, 24-25 March 1999, Napa, California.
11. Measurement Specialties, Inc. Piezo Film Sensors: Technical Manual, 1999.
12. Polyanin, Andrei D., *Handbook of Linear Partial Differential Equations for Engineers and Scientists*. Chapman & Hall/CRC, 2002.
13. Shepherd, Michael J., Richard G. Cobb, William P. Baker. "Clear Aperture Design Criterion for Deformable Membrane Mirror Control," Air Force Institute of Technology (2006).

14. Sobers, D. M. *Smart Structures for Control of Optical Surface*. MS thesis, Air Force Institute of Technology, March 2002.
15. Stamper, Brian, Roger Angel, James Burge, and Neville Woolf. "Flat Membrane Mirrors for Space Telescopes," *SPIE Vol. 4091 Imaging Technology and Telescopes* (2000).
16. Swan Speakers, "Swan Speakers Website." Online at <http://www.swanspeaker.com/product/htm>, February 2006.
17. Trad, Eric M. *Dynamic Characterization of Thin Deformable PVDF Mirror*. MS thesis, Air Force Institute of Technology, March 2002.
18. Vdovin, G., M. Loktev, and A. Simonov. "Low-Cost Deformable Mirrors: Technologies and Goals," *SPIE Vol. 5894 Advanced Wavefront Control: Methods, Devices, and Applications III* (2005).
19. Vuelban, Edgar M., Nandini Bhattacharyn, and Joseph Braat. "A Deformable Mirror Based on Electrocapillary Actuation of a Liquid Surface," *SPIE Vol. 5894 Advanced Wavefront Control: Methods, Devices, and Applications III* (2005).
20. Wang, P. K. C., and F. Y. Hadaegh. "Computation of Static Shapes and Voltages for Micromachined Deformable Mirrors with Nonlinear Electrostatic Actuators," *Journal of Microelectromechanical Systems, Vol 5-3* (1996).
21. Wang, P. K. C., and F. Y. Hadaegh. "Modal Noninteracting Controls for Deformable Mirrors," Proc. of Second IEEE Conference on Control Applications, 13-16 September 1993, Vancouver, British Columbia, Canada.
22. Yang, Eui-Hyeok, and Shcheglov, Kirill. "A Piezoelectric Unimorph Deformable Mirror Concept by Wafer Transfer for Ultra Large Space Telescopes," *SPIE Vol. 4839 Adaptive Optical System Technologies II* (2003).

Vita

John J. Cornelius graduated from high school in May of 1996. From there he went to Embry-Riddle Aeronautical University in Prescott, AZ. He graduated with a Bachelor of Science Degree in Aerospace Engineering in April 2001. While he attended Embry-Riddle, John was a cadet in Air Force ROTC detachment 028.

John was commissioned as a Second Lieutenant in the United States Air Force in May 2001. His first assignment was at the National Air and Space Intelligence Center at Wright-Patterson Air Force Base. While there, he was a foreign space systems engineer developing intelligence products. He promoted to First Lieutenant in May of 2003. His next assignment was at the Air Force Institute of Technology, where he would pursue a Master's of Science degree in Astronautical Engineering.

John promoted to Captain in May of 2005. He will be going to Kirtland Air Force Base in Albuquerque, New Mexico to work at AFRL/DE.

REPORT DOCUMENTATION PAGE

Form Approved
OMB No. 074-0188

The public reporting burden for this collection of information is estimated to average 1 hour per response, including the time for reviewing instructions, searching existing data sources, gathering and maintaining the data needed, and completing and reviewing the collection of information. Send comments regarding this burden estimate or any other aspect of the collection of information, including suggestions for reducing this burden to Department of Defense, Washington Headquarters Services, Directorate for Information Operations and Reports (0704-0188), 1215 Jefferson Davis Highway, Suite 1204, Arlington, VA 22202-4302. Respondents should be aware that notwithstanding any other provision of law, no person shall be subject to a penalty for failing to comply with a collection of information if it does not display a currently valid OMB control number.

PLEASE DO NOT RETURN YOUR FORM TO THE ABOVE ADDRESS.

1. REPORT DATE (DD-MM-YYYY) 23 Mar 06		2. REPORT TYPE Master's Thesis		3. DATES COVERED (From - To) 25 Aug 04 - 23 Mar 06	
4. TITLE AND SUBTITLE 5. Development of In-Plane Surface Deformation Sensing for Thin Film PVDF Actuated Membrane Mirrors				5a. CONTRACT NUMBER	
				5b. GRANT NUMBER	
				5c. PROGRAM ELEMENT NUMBER	
6. AUTHOR(S) Cornelius, John, J., Captain, USAF				5d. PROJECT NUMBER	
				5e. TASK NUMBER	
				5f. WORK UNIT NUMBER	
7. PERFORMING ORGANIZATION NAMES(S) AND ADDRESS(S) Air Force Institute of Technology Graduate School of Engineering and Management (AFIT/EN) 2950 Hobson Way WPAFB OH 45433-7765				8. PERFORMING ORGANIZATION REPORT NUMBER AFIT/GA/ENY/06-M01	
9. SPONSORING/MONITORING AGENCY NAME(S) AND ADDRESS(ES) AFOSR Attn: Lt Col Sharon Heise 4015 Wilson Blvd Rm 713 Arlington VA 22203-1954 DSN: 426-7796				10. SPONSOR/MONITOR'S ACRONYM(S)	
12. DISTRIBUTION/AVAILABILITY STATEMENT APPROVED FOR PUBLIC RELEASE; DISTRIBUTION UNLIMITED.				11. SPONSOR/MONITOR'S REPORT NUMBER(S)	
13. SUPPLEMENTARY NOTES					
14. ABSTRACT This study investigated the feasibility of surface deformation sensing of a membrane mirror using only embedded PVDF sensors. Results were compared to measured deformations using a scanning laser vibrometer. The frequency response function (FRF) was measured based on recorded voltages of a single-layer 7-sensor mirror actuated externally from the embedded PVDF actuators. Additionally, a two-layer, 7-sensor, 7-actuator membrane mirror was constructed for use, with one layer acting as the sensing layer and the other acting as the actuation layer. The measured FRF for this mirror was compared to previous results. Finally a single-layer 61-sensor PVDF mirror was constructed to experimentally investigate the practicality of denser sensor/actuators patterns. Experimental results for all configurations are presented.					
15. SUBJECT TERMS Deformable Mirrors, PVDF, Adaptive Optics, In-plane sensing, In-plane actuation, Zernike Polynomials, Vibrational Modes,					
16. SECURITY CLASSIFICATION OF:		17. LIMITATION OF ABSTRACT	18. NUMBER OF PAGES	19a. NAME OF RESPONSIBLE PERSON	
REPORT	ABSTRACT	c. THIS PAGE	90	Dr. Richard Cobb	
U	U	U		19b. TELEPHONE NUMBER (Include area code) (937) 255-3636, ext 4559; e-mail: richard.cobb@afit.edu	

Standard Form 298 (Rev. 8-98)

Prescribed by ANSI Std. Z39-18